

The Role of Vertical Divergence in Internal Wave/Wave Interactions

Eric Kunze

Applied Physics Laboratory University of Washington, 1013 NE 40th Street, Seattle, WA 98105-6698

Haili Sun

201-2525 NE 195th Street, Seattle, WA 98155

Abstract. Smallscale internal waves are numerically ray-traced through random 3-D Garrett and Munk (GM) internal wave backgrounds. Past ray-tracing investigations have considered only interactions with background vertical shear $V_z = (U_z, V_z)$. Our numerical simulations indicate a non-negligible role for vertical divergence W_z . The spectral transfer of internal-wave energy toward high vertical wavenumber k_z and turbulence production ϵ are 2–4 times shear-only predictions depending on the degree of vertical and horizontal scale-separation imposed. An upper limit is obtained by imposing vertical scale-separation $K_z < k_z$ and no restriction on horizontal wavenumber or frequency. This violates the WKB approximation in the horizontal and time. A lower limit is obtained by imposing stricter vertical scale-separation $K_z < 0.5k_z$ and horizontal scale-separation $K_H < k_h$ for background frequencies $\Omega > 11f$. Imposing WKB horizontal scale-separation at all background frequencies caused some test waves to get stuck at low horizontal wavenumber and low frequency. This is not realistic. The shear-and-strain lower limit produces turbulence production rates close to the upper limit of shear-only calculations and therefore consistent with observations.

1. Introduction

In the stratified ocean interior, internal waves are responsible for most turbulence production and mixing (Eriksen 1978; Munk 1981; Gregg *et al.* 1986; Gregg 1987). The turbulence production rate can be equated to the internal-wave spectral energy transfer rate toward high vertical wavenumber (McComas and Bretherton 1977) $\epsilon_p = \epsilon - \langle w' b' \rangle = (1 + \gamma)\epsilon = (1.0\text{--}1.2)\epsilon$ where the mixing efficiency $\gamma \leq 0.2$ from theory (Osborn 1980; Thompson 1980), laboratory work (McEwan 1983; Itsweire *et al.* 1986) and ocean observations (Oakey 1982). While there has been extensive investigation into the role that internal-wave vertical shear plays in spectral energy transfer in ray-tracing wave/wave simulations (Henyey *et al.* 1986; Gregg 1989), internal-wave vertical divergence has been neglected. In contrast, weak resonant-triad interaction theory (McComas and Müller 1981a, b; McComas and Bretherton 1977; Müller *et al.* 1986) suggests a potentially important role for vertical divergence.

McComas and Bretherton suggested that three classes of interaction dominate wave-triad interactions: (i) *induced diffusion* (ID) due to smallscale high-frequency waves interacting with larger-scale lower-frequency shear, (ii) *elastic scattering* which produces vertical symmetry in the internal wave field but causes

no net spectral energy transfer, and (iii) *parametric subharmonic instability* (PSI) when two smallscale waves interact with a wave of twice their frequency which induces time changes in the buoyancy frequency N through its vertical divergence W_z . Thus, vertical shear plays the major role in induced diffusion, and vertical divergence in parametric subharmonic instability. PSI and ID contribute about 60% and 40% of total spectral energy transfer in weak-triad interactions, respectively. Therefore, weak-triad results suggest that vertical divergence is potentially as important as vertical shear.

A role for high-frequency internal-wave vertical divergence in turbulence production is also implicated in recent oceanic observations. In regions of enhanced high-frequency internal-wave activity adjacent to topography, Padman *et al.* (1991), Wijesekera *et al.* (1993) and Polzin *et al.* (1995) report turbulent dissipation rates elevated above the predictions of the shear-only parameterization of Henyey *et al.* (1986) and Gregg (1989). They suggested that the shear-based parameterization for turbulent dissipation rate ϵ could be corrected with the observed strain variance $\langle \xi_z^2 \rangle$ to capture the high-frequency wave dynamics. However, in vertical wavenumber ray-tracing equation (2.4), it is vertical divergence W_z , not strain ξ_z , which contributes

to the time rate of change of vertical wavenumber. We will examine the role of the vertical divergence term in the ray-tracing equations more closely.

Two finescale parameterizations for the turbulent dissipation rate ϵ developed for GM model spectral shapes have displayed some skill in reproducing ocean observations. The first is based on weak-triad interaction theory (McComas and Bretherton 1977; McComas and Müller 1981a, b) and the second on an eikonal (ray-tracing) interaction approach (Henyei *et al.* 1986). These agree with fine- and microstructure observations of the ocean (Gregg 1989; Polzin *et al.* 1995) in their dependence on spectral level E^2 and buoyancy frequency N^2 . But, when both models are adjusted to a Munk (1981) model spectrum, Henyei *et al.*'s predicted dissipation rate is 3–4 times weaker than the weak-triad rate.

1.1 McComas and Müller (1981b, MM)

Internal-wave spectral energy transfer rates from large to small scales can be calculated directly for each interaction triad,

$$Q_{\text{psi}} = \frac{E}{\tau_{\text{psi}}} \quad Q_{\text{id}} = \frac{E}{\tau_{\text{id}}}$$

where E is the canonical spectral energy density of the wave field, and τ_{psi} and τ_{id} are characteristic timescales of parametric subharmonic instability and induced diffusion, respectively. For a GM76 internal-wave spectra (Cairns and Williams 1976), McComas and Müller (1981b) predicted that the spectral energy transfer toward small scales (equivalent to the steady-state turbulence production rate) would be

$$\begin{aligned} \epsilon_{\text{MM}} = Q_{\text{psi}} + Q_{\text{id}} = & \left(\frac{27\pi}{32\sqrt{10}} + 1 \right) \\ & \times \pi^2 b^2 j^{*2} f N^2 E_{\text{GM}}^2 \end{aligned} \quad (1.1)$$

where $b = 1300$ m is the pycnocline's stratification lengthscale, f the Coriolis frequency, j^* the peak mode number, N the buoyancy frequency and E_{GM} the dimensionless spectral energy level (Table 1). Resonant-triad theory requires that the decorrelation time of the wave field be shorter than its interaction time (Müller *et al.* 1986) so that interactions must be weak.

1.2 Henyei, Wright and Flatté (1986, HWF)

Henyei *et al.* (1986) explored internal wave/wave interactions using ray tracing to overcome the questionable validity of weak interaction assumptions for finescale oceanic internal waves (Holloway 1980). This approach

is referred to as *strong* wave/wave interaction **Table 1**. Parameters in the Garrett and Munk internal wave model spectrum (Munk 1981).

$f = 7.3 \times 10^{-5} \text{ rad s}^{-1}$	Coriolis frequency at 30°N
$N_0 = 72f = 5.3 \times 10^{-3} \text{ rad s}^{-1}$	reference buoyancy frequency
$N(z) = N_0 e^{z/b}$	depth-dependent mean buoyancy frequency (z positive upward)
$N_i(x, y, z, t)$	instantaneous buoyancy frequency
$b = 1300 \text{ m}$	scale depth of thermocline
$E_{\text{GM}} = 6.3 \times 10^{-5}$	midlatitude dimensionless energy level
$j^* = 3$	peak vertical mode number
$k_{z_c} = \frac{1}{3 j^* b E_{\text{GM}} Ri_c^{-1}} \text{ m}^{-1}$	high vertical wavenumber cutoff
$Ri_c = 2$	Richardson number at the cutoff vertical wavenumber k_{z_c}

by Müller *et al.* (1986) because it places no restrictions on the ratio of the decorrelation and interaction times in the wave field. However, ray tracing requires that (i) WKB scale-separated ($K_i < k_i$, $\Omega < \omega$) wave/wave interactions dominate, and (ii) the smallscale waves not significantly modify the larger-scale background. The internal-wave spectral energy transfer is calculated following smallscale test waves' propagation in a larger-scale background wave field described by the Garrett and Munk model spectrum (Munk 1981). Only interactions with background internal-wave vertical shear were presumed important in Henyei *et al.*'s (1986) calculations. They did not apply WKB scale-separation in time or the horizontal. They derived a parameterization for ϵ based on the spectral energy transfer rate toward high vertical wavenumber k_z

$$\epsilon(k_z) = \int S[E](k_z, \omega) \left\langle \frac{dk_z}{dt} \right\rangle d\omega \quad (1.2)$$

in terms of the energy spectra $S[E](k_z, \omega)$ and the ensemble-average time rate of change of vertical wavenumber k_z . The ray-tracing equation for vertical wavenumber k_z , including only vertical shear interactions, was expressed in terms of rms shear

$$\left\langle \frac{dk_z}{dt} \right\rangle = \left\langle \frac{\partial(k_h \cdot \mathbf{V})}{\partial z} \right\rangle \sim \sqrt{k_h^2 \langle V_z^2 \rangle} \langle \cos^2 \theta \rangle$$

$$\approx \frac{k_h N}{\sqrt{2Ri_c}} \sqrt{1 + \ln(k_z/k_{zc})} \quad (1.3)$$

where k_h is the horizontal wavenumber, θ the orientation of the horizontal wavevector, k_{zc} , the vertical wavenumber of the finescale change in spectral slope ($= 0.08$ cpm in the GM model), and Ri_c the corresponding Richardson number. Finally, they derive a parameterization for the turbulent dissipation rate ϵ in a Munk (1981) GM internal-wave field

$$\epsilon_{\text{HWF}} = \frac{12 Ri_c^{1/2} b^2 j^{*2} f N^2 E_{\text{GM}}^2 \left(\frac{k_{zc}}{k_z}\right)^2}{\sqrt{2\pi}} \times \sqrt{1 + \ln\left(\frac{k_z}{k_{zc}}\right)} \left(\frac{1-r}{1+r}\right) \text{Arccosh}\left(\frac{N}{f}\right) \quad (1.4)$$

where $r(k_z)$ is the ratio of up- to downscale spectral energy flux at vertical wavenumber k_z .

1.3 Gregg (1989)

Gregg (1989) introduced parameterizations for ϵ using 10-m vertical shear as a measure of the internal-wave energy level, that is, replacing E_{GM}^2 in McComas and Müller (1981b) and Henyey *et al.* (1986) with $\langle E_{\text{IW}}^2 \rangle = E_{\text{GM}}^2 \langle S_{10}^2 / S_{\text{GM}}^2 \rangle$ where S_{GM}^2 is the 10-m GM shear variance, $S_{10}^2 = 2.11 [(\Delta U / \Delta z)^2 + (\Delta V / \Delta z)^2]$ the measured 10-m shear variance, $\Delta z = 10$ m and the 2.11 multiplier corrects for attenuation by the first-difference filter. With the assumption that $\langle S_{10}^4 \rangle = 2 \langle S_{10}^2 \rangle^2$ and $\langle S_{\text{GM}}^4 \rangle = 2 \langle S_{\text{GM}}^2 \rangle^2$, he rewrote McComas and Müller's (1981b) and Henyey *et al.*'s (1986) formulas as

$$\epsilon_{\text{MM}} = 1.1 \times 10^{-9} \frac{\langle N^2 \rangle \langle S_{10}^2 \rangle^2}{N_0^2 \langle S_{\text{GM}}^2 \rangle^2} \quad (\text{W kg}^{-1}) \quad (1.5)$$

$$\epsilon_{\text{HWF}} = 0.35 \times 10^9 \frac{\langle N^2 \rangle \langle S_{10}^2 \rangle^2}{N_0^2 \langle S_{\text{GM}}^2 \rangle^2} \quad (\text{W kg}^{-1}) \quad (1.6)$$

where we have adjusted ϵ_{MM} to be consistent with the Munk (1981) GM model spectrum used throughout this paper. The rewritten Henyey *et al.* (1986) model (1.6) collapsed PATCHEX and RING 82-I data sets to within a factor of two.

Gargett (1990) pointed out that the method used by Gregg (1989) to calculate the wave energy level E would underestimate E for $E > E_{\text{GM}}$ if Ek_{zc} is constant (Smith *et al.* 1987; Duda and Cox 1989). In addition,

neither frequency nor wavenumber information were provided, so it is difficult to evaluate if and how the observations deviate from GM. Polzin *et al.* (1995) conjectured that ‘‘Gregg was able to collapse his PATCHEX and RING 82-I data sets under the $E^2 N^2$ scaling due to a cancellation between the underestimation of E and lower-than-expected dissipations associated with lower-than-average wave frequency.’’

1.4 Polzin *et al.* (1995)

Polzin *et al.* (1995) modified Henyey *et al.*'s (1986) formula following Henyey (1991) by rewriting (1.2) so that the spectral energy-flux through a fixed wavenumber can be estimated as

$$\epsilon(k_z) = \frac{1}{2k_z^2} \{S[V_z](k_z) + N^2 S[\xi_z](k_z)\} \times \left\{ \int_0^{k_z} S[V_z](k_z) dk_z \right\}^{1/2} \times k_z \left\langle \sqrt{\frac{\omega^2 - f^2}{N^2 - \omega^2}} \right\rangle_E \times \frac{1}{\sqrt{2}} \left(\frac{1-r(k_z)}{1+r(k_z)} \right) \quad (1.7)$$

where $\langle \cdot \rangle_E$ is the expected value, $S[V_z](k_z)$ and $S[\xi_z](k_z)$ correspond to the GM76 (Cairns and Williams 1976; Gregg and Kunze 1991) vertical wavenumber spectra for shear and strain, and $k_z^{-2} \{S[V_z](k_z) + N^2 S[\xi_z](k_z)\} / 2$ collapses the total energy spectra

$$\int_f^N S[E](k_z, \omega) d\omega.$$

Other terms in (1.7) come from rewriting the ray-tracing equation for vertical wavenumber k_z (2.4). The expected value for

$$\left\langle \frac{\sqrt{\omega^2 - f^2}}{\sqrt{N^2 - \omega^2}} \right\rangle_E$$

was estimated by Polzin *et al.* (1995) using the shear-to-strain variance ratio for a single internal wave,

$$R_\omega = \frac{S[V_z](k_z)}{N^2 S[\xi_z](k_z)} = \frac{(\omega^2 + f^2)(N^2 - \omega^2)}{N^2(\omega^2 - f^2)}$$

which yields a biased estimator for frequency

$$\omega^2 = \frac{1}{2} \left[N^2(1 - R_\omega) - f^2 + \sqrt{N^4(R_\omega - 1)^2 + 2f^2 N^2(1 + 3R_\omega) + f^4} \right]$$

(Appendix B of Polzin *et al.* 1995). Polzin *et al.* showed that the modified model (1.7) collapsed, to within a factor of two, data sets in both GM and weakly non-GM backgrounds.

1.5 Summary and Preamble

Using ray-tracing simulations, this paper formulates parameterizations for the turbulent production rate including interactions with both shear and vertical divergence. We restrict our analysis to Munk (1981) GM spectral shapes for comparison with Henyey *et al.*'s results. Our ray-tracing estimates of internal-wave spectral energy transfer imply turbulence dissipation rates ϵ that are 2–4 times those without vertical divergence (see Fig. 10 in Sec. 5.2) depending on the degree of scale-separation imposed between background and test waves.

WKB scale-separations are applied to get upper and lower limits for the spectral energy transfer rate. An upper limit is obtained by restricting the vertical wavenumbers of the background to be lower than those of the test waves ($K_z < k_z$) following Henyey *et al.* (1986). While this allows interactions with horizontal wavenumbers and frequencies that do not meet the WKB criterion, we include these for comparison with previous shear-only calculations. To get a lower limit, the background vertical wavenumber is restricted to be at most half that of the test wave ($K_z < 0.5k_z$), and the background horizontal wavenumber restricted to be lower than that of the test wave ($K_H < k_h$) for background frequencies $\Omega > 11f$. Applying WKB scale-separation in the horizontal at all frequencies or in frequency ($\Omega < \omega$) results in some test waves getting stuck at low horizontal wavenumber and frequency with no background to interact with. This is not realistic. The lower-limit criteria given above are a compromise in that wave frequencies $\Omega < 11f$ encompass 95% of the shear and 90% of the strain variance. It allows test waves to cascade to the small scale but omits the highest frequency contributions from the background.

Ray-tracing will not handle the upper-limit case accurately because the WKB approximation becomes questionable as the scales of the background and wave become comparable, and is invalid when test-wave scales are much larger than those of the background. Interactions with background waves with vertical scales comparable to the test waves ($k_z/2 < K_z < k_z$) account for a third of the total spectral energy transfer toward high wavenumber. This suggests that strong finescale wave/wave interactions do modify the background finescale field so the requirement that test waves not modify the background becomes questionable on the finescale. The factor of 2–4 uncertainty between the

upper- and lower-limit estimates is comparable to the factor-of-two uncertainty in observations. Since very rapid fluctuations in the background should not contribute to the longterm evolution of test waves, we favor the lower-limit estimates for the turbulent production rate but caution that they may under- or overestimate the contribution from the finescale ($K_z \sim k_z$). Observations favor the lower limit (see Fig. 14 in Sec. 6) except in data from the slope of a seamount where the frequency spectrum is decidedly non-GM (Eriksen 1998).

2. Ray-Tracing Equations

In this section, we examine the WKB ray-tracing equations for internal wave/wave interactions using the GM internal wave model (Munk 1981). The ray-tracing equations for tracking the evolution of smallscale test wavepackets' wavevector $\mathbf{k} = (k_x, k_y, k_z)$ and position $\mathbf{r} = (x, y, z)$ in a slowly-varying background are

$$\frac{D\mathbf{r}}{Dt} = \frac{\partial\omega_E}{\partial\mathbf{k}} = \frac{\partial\omega_i}{\partial\mathbf{k}} + \mathbf{V} = \mathbf{Cg} + \mathbf{V} \quad (2.1)$$

$$\frac{D\mathbf{k}}{Dt} = \nabla\omega_E = \frac{\partial\omega_i}{\partial N_i} \nabla N_i - \nabla(\mathbf{k} \cdot \mathbf{V}) \quad (2.2)$$

$$\frac{D\omega_E}{Dt} = \frac{\partial\omega_E}{\partial t} = \frac{\partial\omega_i}{\partial N_i} \frac{\partial N_i}{\partial t} - \mathbf{k} \cdot \frac{\partial\mathbf{V}}{\partial t} \quad (2.3)$$

(Lighthill 1978) where D/Dt is the time rate of change following the wave packet, $\omega_E = \omega_i + \mathbf{k} \cdot \mathbf{V}(\mathbf{r}, t)$ the wavepacket's Eulerian frequency, $\omega_i(N_i, f, \mathbf{k})$ its intrinsic (Lagrangian) frequency, $\nabla = (\partial/\partial x, \partial/\partial y, \partial/\partial z)$ a partial operator, \mathbf{V} the background wave-induced velocity and N_i the background instantaneous buoyancy frequency. The internal-wave intrinsic frequency is presumed to obey the linear intrinsic dispersion relation

$$\omega_i^2 = \frac{N_i^2 k_H^2 + f^2 k_z^2}{k^2}$$

where $k_H = \sqrt{k_x^2 + k_y^2}$ is the test wave's horizontal wavenumber. The intrinsic dispersion relation appears in the first terms of ray-tracing equations (2.1)–(2.3), that is, in terms of the form $\partial\omega_i/\partial(\mathbf{k}, \mathbf{r}, t)$. Finescale internal waves have very slow group velocities so their dispersion proves irrelevant compared to advection (see Appendix A and Fig. A1). Numerical simulations in which the fine-scale group velocity was either reduced or reversed [$\mathbf{Cg} = (0.1, -1)\mathbf{Cg}_{\text{IW}}$ for $\lambda_z \leq 20$ m] while larger wavelengths propagated at their linear speed ($\mathbf{Cg} = \mathbf{Cg}_{\text{IW}}$ for $\lambda_z \geq 100$ m) produce spectral energy transfer rates indistinguishable from those using the linear dispersion

relation above. Including the instantaneous N_i rather than mean \bar{N} also does not modify test-wave evolution significantly. This suggests that the choice of finescale test-wave dispersion relation is unimportant. The net spectral transfer of energy toward high vertical wavenumber is controlled by Doppler shifting and so depends more on the aspect ratio λ_z/λ_H of finescale variability than its intrinsic frequency. Thus, potential-vorticity-carrying finestructure (vortical mode) should be transferred toward high vertical wavenumbers at the same rate as finescale internal waves of the same aspect ratio (see also Haynes and Anglade 1997).

The ray-tracing equation for a test wavepacket's vertical wavenumber (2.4) can be expanded to

$$\boxed{\frac{dk_z}{dt} = -\frac{\partial\omega_E}{\partial z} = -k_x \frac{\partial U}{\partial z} - k_y \frac{\partial V}{\partial z} - k_z \frac{\partial W}{\partial z} - \frac{\partial\omega_i}{\partial N_i} \frac{\partial N_i}{\partial z}} \quad (2.4)$$

I I II III

where

$$\frac{\partial\omega_i}{\partial N_i} = \frac{N_i k_H^2}{\omega_i k^2}. \quad (2.5)$$

The WKB approximation requires that test-wave wavelengths λ be much smaller than those of the background Λ ($\lambda < \Lambda/2\pi$).

Scale analysis of vertical ray-tracing equation (2.4) would suggest that (i) the vertical shear \mathbf{V}_z term, contributed mostly by near-inertial waves, dominates the evolution of high-frequency test waves, (ii) the vertical divergence W_z term, contributed by higher-frequency waves, dominates the evolution of near-inertial test waves, and (iii) the vertical buoyancy frequency gradient term can be neglected for all test-wave frequencies. Conclusions about the role of vertical divergence are qualitatively unchanged when high-frequency, high-horizontal-wavenumber contributions to the vertical divergence are excluded.

3. Numerical Simulations

3.1 The Background Wave Field

To numerically ray-trace smallscale waves in a larger-scale internal wave background, we first set up the background field. Following Henyey *et al.* (1986), the background wave field is based on the Munk (1981) version of the Garrett and Munk model spectrum in (Ω, K_z) -space

$$S[\mathbf{V}](\Omega, \mathbf{j}, z) = \frac{2b^2 NN_0 E_{GM}}{\pi f} \times \frac{(j^2 + j_*^2)^{-1}}{\sum_{j=1}^{\infty} (j^2 + j_*^2)^{-1}} \frac{\Omega^2 + f^2}{\Omega^3 \sqrt{\Omega^2 - f^2}} \quad (3.1)$$

where the parameters are defined in Table 1. Vertical wavenumber K_z is related to the mode number j by

$$K_z = \frac{\pi j}{b} \sqrt{\frac{N^2 - \Omega^2}{N_0^2 - \Omega^2}}.$$

The Monte-Carlo method is used to set up random GM backgrounds (Appendices B and D). Ensemble results will use up to 100 randomly generated backgrounds to ensure that all phases of the background wave field are sampled uniformly by the initial test waves, and to obtain statistical stability. Following Henyey *et al.* (1986), the wave frequency $f \leq \Omega \leq N$, mode number j , amplitude \mathbf{V}_0 , and horizontal wavevector direction $\theta = \text{Arctan}(K_y/K_x)$ are all randomly selected (Appendix B) so that the simulated background horizontal velocity field \mathbf{V} is (i) 4-D, varying in time and space, (ii) horizontally isotropic and (iii) in agreement with GM.

Background vertical shear $\mathbf{V}_z = (U_z, V_z)$, vertical divergence W_z , strain ξ_z and instantaneous buoyancy frequency N_i are derived from the horizontal velocity using linear internal-wave consistency relations (Fofonoff 1969)

$$\mathbf{V}_z = (U_z, V_z) = iK_z \mathbf{V}$$

$$W_z = -i(K_x U + K_y V)$$

$$\xi_z = \frac{1}{\Omega}(K_x U + K_y V)$$

$$N_i^2 = \bar{N}^2(z) [1 + \xi_z]$$

(Appendix D). The Monte-Carlo simulated spectra agree with GM (Fig. 1).

3.2 Coordinate Transformation

The GM model is a spectrum of Eulerian dependent variables (e.g., \mathbf{V} , ξ , N_i) set in a Lagrangian coordinate frame [e.g., independent-variable particle labels x' , y' , $z'(\rho)$], that is, in a coordinate system following water parcels. Observations have shown that, although the ω^{-2} GM model does not describe the almost-flat finescale ($\lambda_z \simeq 10\text{--}50$ m) Eulerian frequency spectra for shear and strain (Pinkel 1984), it better describes spectra transformed into an isopycnal-following (or semi-

Lagrangian) frame (Sherman and Pinkel 1991; Anderson 1993). In an Eulerian description, internal-wave shear and vertical divergence vary rapidly in time due to finestructure being swept past a fixed position by large-scale background velocities. Since finescale waves are advected with the background, such an Eulerian coordinate system is inappropriate for the test waves. In order to include background vertical divergence in ray-tracing calculations without Doppler-shift aliasing of high-wavenumber structure, we need either to (i) transform equations (2.1–2.2) into a Lagrangian frame or (ii) transform the Lagrangian particle label variables $x', y', z'(\rho), t'$ in \mathbf{V} and N_i into Eulerian variables (Henye personal communication 1999). As in Henye *et al.* (1986), we choose to transform the ray-tracing equations into a semi-Lagrangian frame (i) following vertical but not horizontal displacements by background waves (Appendix C), so that neither (i) nor (ii) are applied horizontally.

3.3 Numerical Simulation Results

Before looking at ensemble statistics, we examine a few typical test-wave trajectories selected from 100 runs. In the following simulations, we take the unperturbed buoyancy frequency to be constant, $\bar{N} = 40f = 2.9 \times 10^{-3} \text{ rad s}^{-1}$, which approximates the average buoyancy frequency in the upper ocean. We initialize the test-wave horizontal wavenumbers to be $k_{x_0} = 0.025 \text{ rad m}^{-1}$ and $k_{y_0} = 0$. Test waves interact with the total GM vertical divergence in these calculations so will overestimate the role of divergence.

3.3.1 Typical test-wave trajectories. Following a typical test-wave trajectory (initially at $\omega_i = 9f$, $k_{z_0} = 0.12 \text{ rad m}^{-1}$), Fig. 2 illustrates the evolution of test-wave

- (a) vertical wavenumber k_z ,
- (b) intrinsic frequency ω_i ,
- (c) contributions to the time rate of change of k_z by the zonal shear $k_x U_z$, vertical divergence

- $k_z W_z$ and buoyancy frequency gradient $(\partial\omega_i/\partial N_i)(\partial N_i/\partial z)$ terms in (2.4),
- (d) their cumulative counterparts $\langle k_x U_z \rangle_t$, $\langle k_z W_z \rangle_t$ and $\langle (\partial\omega_i/\partial N_i)(\partial N_i/\partial z) \rangle_t$, and encountered background
- (e) shear magnitude $|\mathbf{V}_z|$,
- (f) buoyancy frequency anomaly $\delta N = N_i - N$, and
- (g) vertical divergence W_z

where interactions with *total* background shear \mathbf{V}_z , vertical divergence W_z and buoyancy frequency perturbations $\partial N_i/\partial z$ are allowed. When a test wave has low intrinsic frequency ($\omega_i < 4f$), evolution of its vertical wavenumber (8–12 h, Fig. 2c) is controlled mostly by the background vertical divergence term $k_z W_z$. When it has high frequency ($\omega_i > 16f$), the background shear term $k_x U_z$ dominates its behavior (1–3 h, Fig. 2c). For intermediate test-wave frequencies, background vertical divergence and shear have comparable contributions (3–6 h, Fig. 2c). The cumulative vertical divergence term $\langle k_z W_z \rangle_t$ is twice the cumulative vertical shear $\langle k_x U_z \rangle_t$ term, indicating that, despite being dominated by near-buoyancy frequencies, the vertical divergence term has a significant net impact over the lifespan of a test wave. We caution that these simulations include vertical divergence contributions that are not WKB scale-separated in the horizontal or time. The buoyancy frequency gradient term $\langle (\partial\omega_i/\partial N_i)(\partial N_i/\partial z) \rangle_t$ is everywhere negligible.

Figure 3 displays the evolution of

- (a) test-wave vertical wavenumber k_z ,
- (b) intrinsic frequency ω_i ,
- (c) the zonal shear term $k_x U_z$ in (2.4),
- (d) its cumulative form $\langle k_x U_z \rangle_t$, and
- (e) encountered background shear \mathbf{V}_z

in the same background as Fig. 2 but allowing interactions only with vertical shear \mathbf{V}_z . In this case, only background shear transfers test waves to smaller scale. It takes three times as long for the test wave's vertical wavelength to fall below 5 m in the absence of vertical divergence interactions.

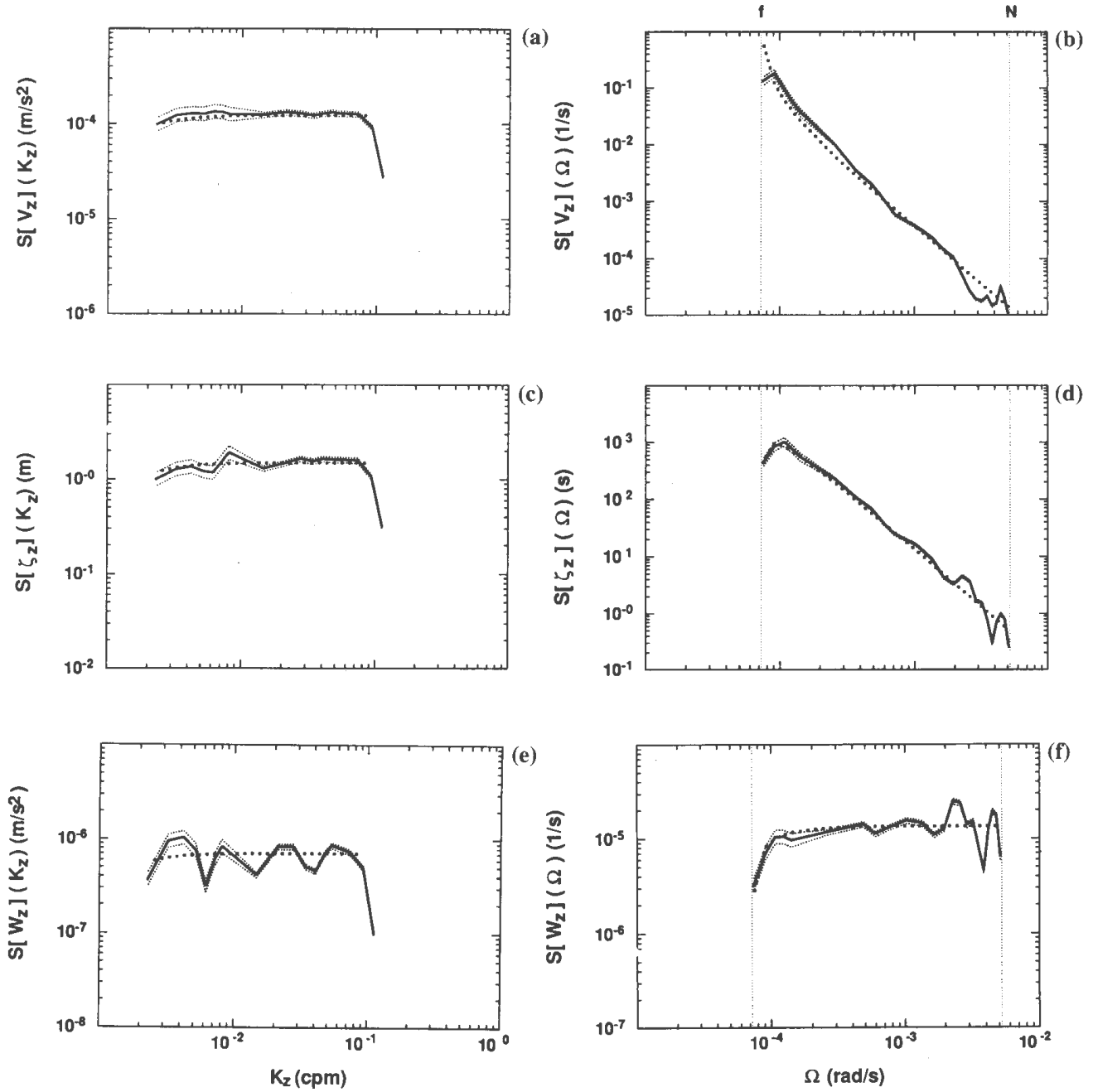


Figure 1. Monte-Carlo-simulated background GM internal-wave spectra (solid curves with 95% confidence limits as thin dotted curves) for vertical shear as functions of vertical wavenumber $S[V_z](K_z)$ (a) and frequency $S[V_z](\Omega)$ (b), strain spectra as a functions of vertical wavenumber $S[\zeta_z](K_z)$ (c) and frequency $S[\zeta_z](\Omega)$ (d), and vertical divergence spectra as a functions of vertical wavenumber $S[W_z](K_z)$ (e) and frequency $S[W_z](\Omega)$ (f). The simulated spectra agree well with the GM model (thick dotted).

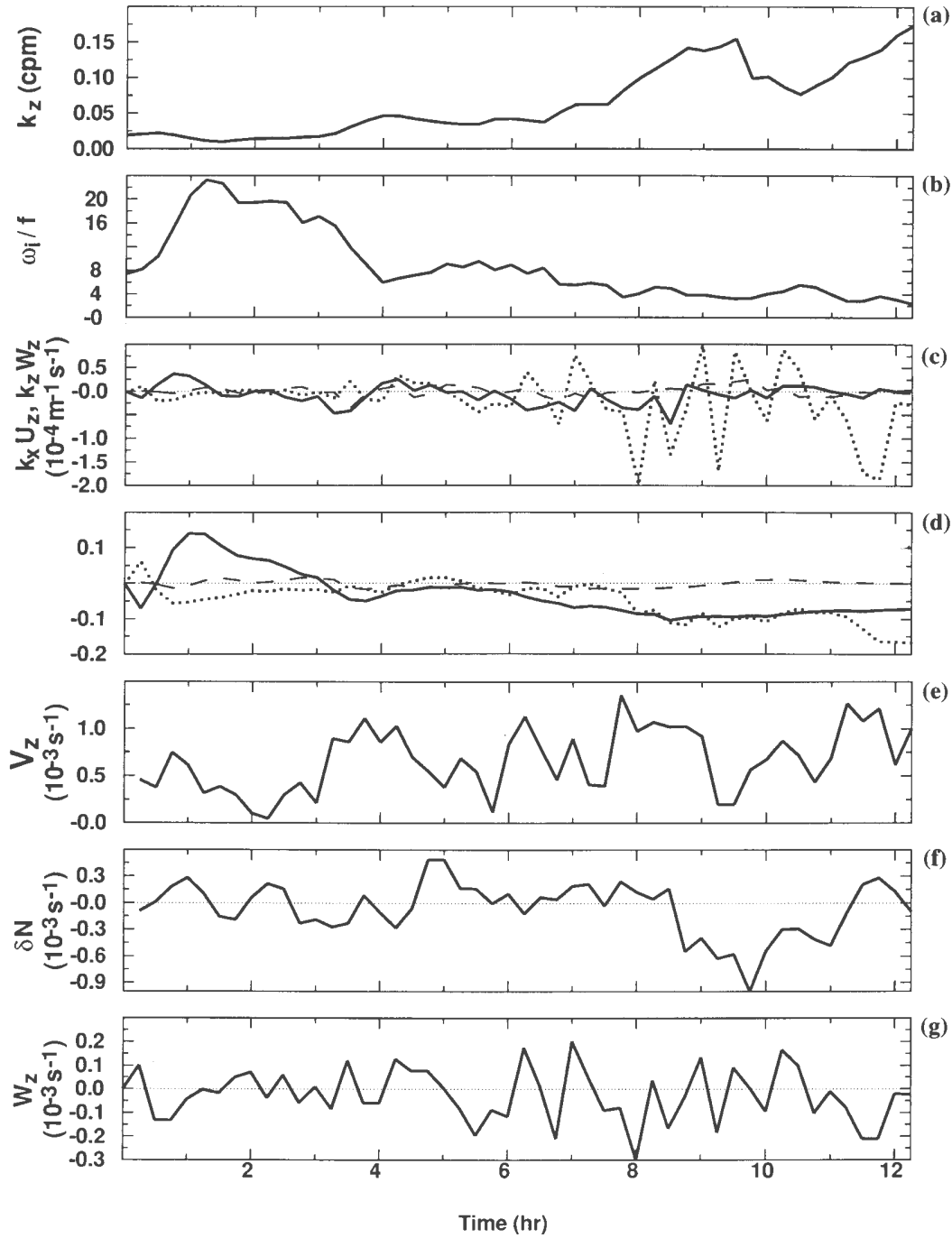


Figure 2. Following the evolution of a typical test wave in a GM background filtered only by vertical wavenumber ($K_z < k_z$). Panels display the evolution of test-wave vertical wavenumber k_z (a), intrinsic frequency ω_i (b), contributions to dk_z/dt from vertical shear $k_x U_z$ (solid), vertical divergence $k_z W_z$ (dashed) and vertical buoyancy frequency gradients $(\partial\omega_i/\partial N_i)(\partial N_i/\partial z)$ (dotted) (c), cumulative contributions $\langle k_x U_z \rangle_t$ (solid), $\langle k_z W_z \rangle_t$ (dashed) and $\langle (\partial\omega_i/\partial N_i)(\partial N_i/\partial z) \rangle_t$ (dotted) (d), encountered background shear magnitude $|V_z|$ (e), buoyancy fluctuations $\delta N = N_i - N$ (f), and vertical divergence W_z (g). Initial conditions for the test wave are $\omega_i = 9f$, $k_z = 0.12 \text{ rad m}^{-1}$, $k_x = 0.025 \text{ rad m}^{-1}$ and $k_y = 0$. The test wave interacts with background vertical shear V_z ,

vertical divergence w_z and vertical buoyancy frequency gradient $(\partial\omega_z/\partial N_i)(\partial N_i/\partial z)$. The background rms shear $\sqrt{\langle V_z^2 \rangle} = 1.83 \times 10^{-3} \text{ s}^{-1}$, rms vertical divergence $\sqrt{\langle W_z^2 \rangle} = 0.14 \times 10^{-3} \text{ s}^{-1}$, and rms strain $\sqrt{\langle \xi_z^2 \rangle} = 0.4$.

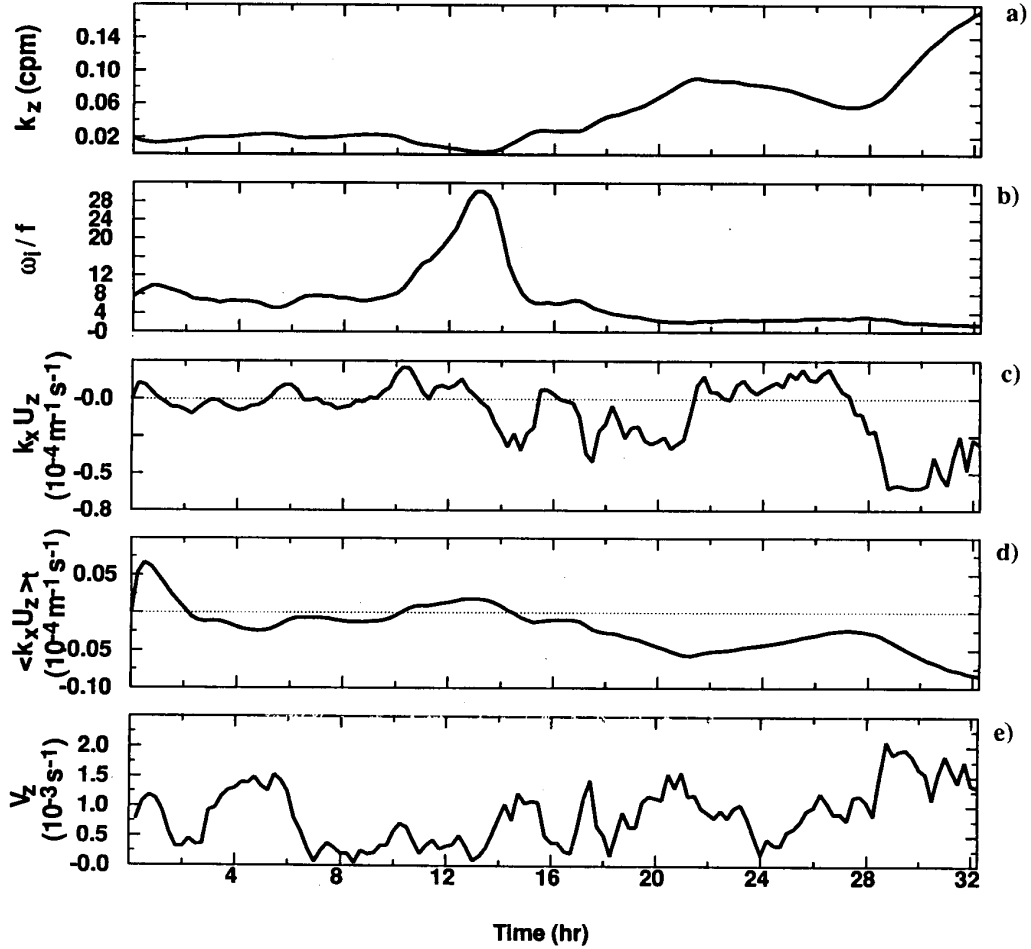


Figure 3. For the same initial conditions as in Fig. 2 but allowing interactions only with the background vertical shear V_z . The panels show evolution of test-wave vertical wavenumber k_z (a), intrinsic frequency ω_i (b), contributions to dk_z/dt from $k_x U_z$ (c), its cumulative counterpart $\langle k_x U_z \rangle_t$ (d), and background shear magnitude $|V_z|$ (e). Test-wave behavior differs from that in Fig. 2, taking longer to reach small vertical scales.

3.3.2 Statistics. In the following, we present ensemble results based on test waves propagating in over 100 different Monte-Carlo backgrounds in order to sample the range of random phases and fluctuations present in the ocean and obtain stable statistics.

3.3.2.1 Test-wave breaking frequency. Figures 4 and 5 display histograms of test-wave intrinsic frequency at the instant their vertical wavelengths λ_z fall below the “breaking” wavelength of 5 m. Test-wave breaking histograms are independent of initial test-wave frequency (Fig. 4), implying an equilibrium finescale fre-

quency spectrum. The histograms fall off more gently than the expected ω_i^{-1} distribution for an ω_i^{-2} spectrum (dotted curves), indicating that, for interactions involving all shear and vertical divergence, ray tracing suggests a gentler equilibrium spectral slope than GM. In Fig. 5, simulations are considered which include interactions with (a) only background shear, (b) both background shear and vertical divergence, and (c) both background shear and vertical divergence but imposing frequency scale-separation $\Omega < \omega_i$ between the test wave and the background. Test waves that stall at low

horizontal wavenumber because of the frequency scale-separation are not included in the statistics of (c). When only interactions with shear (a), or when frequency scale-separation (c), are imposed, test-wave breaking is more tightly confined to near-inertial frequencies, implying a test-wave spectral energy-flux toward low frequency and high vertical wavenumber. Figure 5c indicates that background vertical divergence plays an order-one role only when its frequency is

higher than the test-wave intrinsic frequency. In strict WKB scale-separation, this would imply that only shear drives a spectral energy transfer to high vertical wavenumber. But this contradicts observations of turbulent mixing in excess of that predicted by shear-only models in the presence of elevated high-frequency internal waves (Wijesekera *et al.* 1993; Polzin *et al.* 1995).

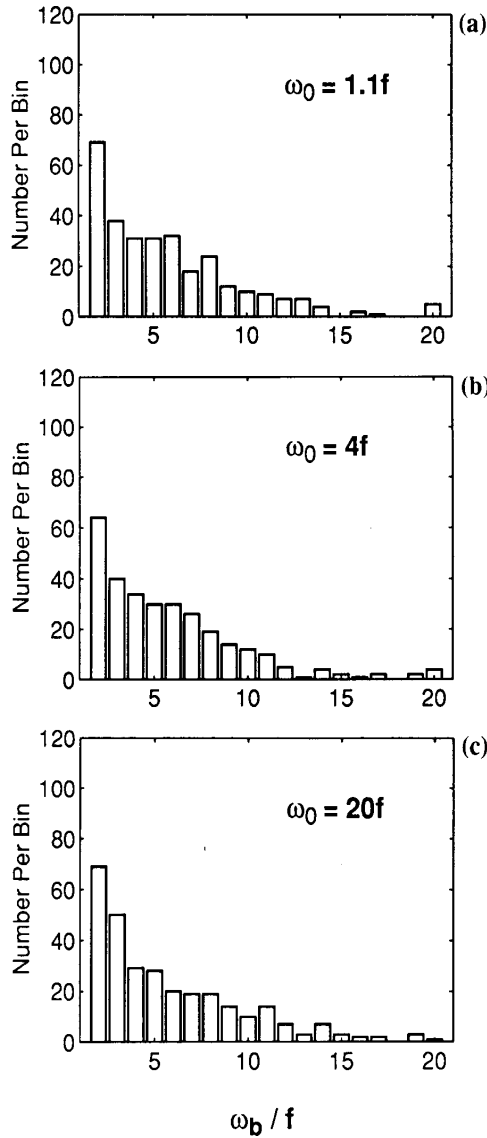


Figure 4. Histograms of the test-wave breaking frequencies for initial test-wave frequencies (a) $\omega_i = 1.1f$, (b) $\omega_i = 4f$ and (c) $\omega_i = 20f$. The histograms are independent of initial test-wave frequency.

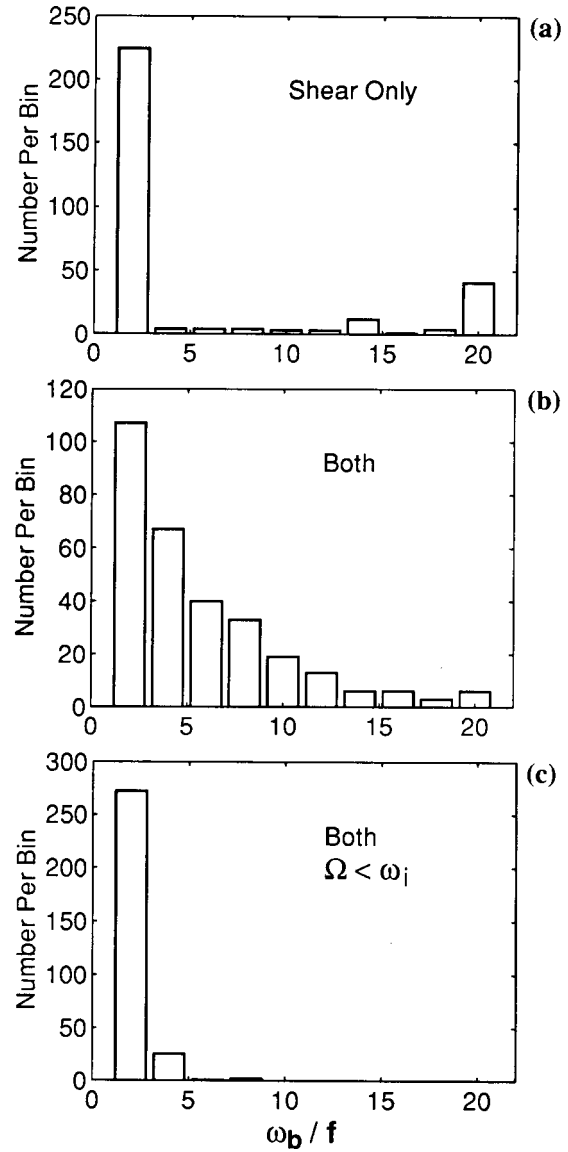


Figure 5. Histograms of test-wave frequencies at the instant of breaking ($\lambda_z < 5$ m) for test waves interacting with (a) only background shear, (b) both shear and vertical divergence, and (c) both shear and vertical divergence but restricting interactions to background frequencies lower than the test waves' ($\Omega < \omega_i$). Test waves are initialized with intrinsic frequencies $\omega_i = 21f$ and vertical wavenumbers $k_z = 0.05$ rad m^{-1} . Test waves

interacting with vertical divergence as well as vertical shear (b) break at higher frequencies than those interacting with shear only (a). However, if frequency scale-separation is imposed between the test waves and background ($\Omega < \omega_i$) (c), the histograms of breaking frequency with and without vertical divergence are similar.

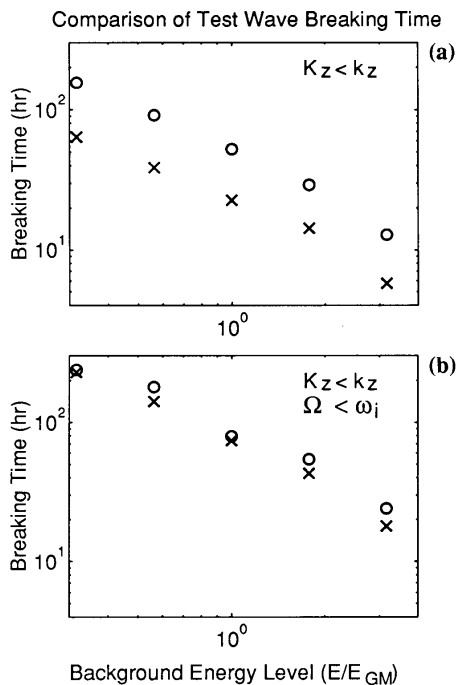


Figure 6. Test-wave lifespans (while $\lambda_z > 5$ m) versus background energy level E without (a) and with (b) frequency scale-separation ($\Omega < \omega_i$). Test waves are initialized with intrinsic frequencies $\omega_i = 9f$ and vertical wavenumbers $k_z = 0.12 \text{ rad m}^{-1}$. The “x” denotes average test-wave lifespans for interactions with both background vertical divergence and shear, and “o” for interactions only with shear. The difference in lifespans with and without vertical divergence is a constant ratio of 2, independent of the background energy level (a). With frequency separation ($\Omega < \omega_i$) (b), test-wave lifespans are little affected by vertical divergence interactions.

3.3.2.2 Test-wave lifespans. Figure 6 shows test-wave lifespans (while $\lambda_z > 5$ m) versus background spectral energy level E without (a) and with (b) frequency scale-separation $\Omega < \omega_i$ between the test wave and background. Each average includes simulations with 100 different backgrounds. Again, test waves that get stuck at low horizontal wavenumber are excluded from the statistics of Fig. 6b. The difference in average lifespan $\langle \Delta t \rangle$ between simulations with and without vertical divergence interactions is a constant ratio of ~ 2 , independent of the background energy level (Fig. 6a). Increasing the background energy level causes the

breaking time to decrease smoothly. Consistent with Fig. 5c, imposing WKB frequency scale-separation ($\Omega < \omega_i$) results in almost identical average test-wave lifespans with and without background divergence W_z interactions.

Test-wave lifespans and frequencies at the time of breaking (when λ_z falls below 5 m) are not sensitive to the number of waves comprising the background, provided the background wave field reproduces the GM model spectrum (Fig. 7). Turbulence production rates $\epsilon(1 + \gamma)$ should likewise be insensitive to the exact number of waves making up the background.

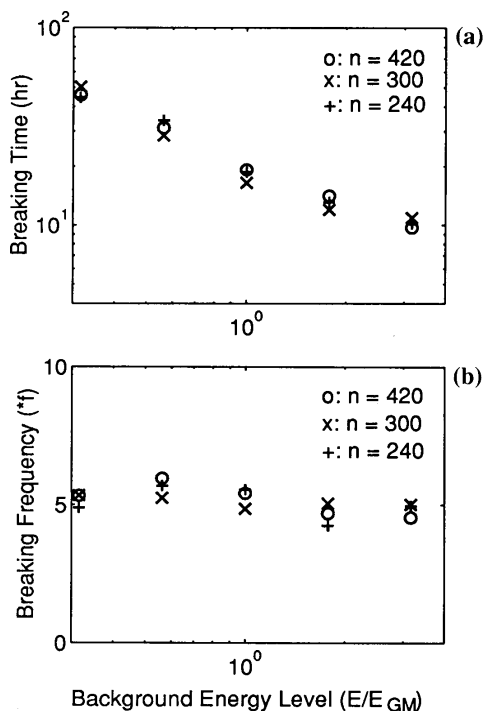


Figure 7. Test-wave lifespans (a) and frequencies (b) as a function of spectral energy level E/E_{GM} at the time λ_z falls below 5 m for different numbers of waves comprising the background. Test-wave lifespans and frequencies are insensitive to the number of background waves NW provided the background wave field reproduces the GM model spectrum.

The above conclusions are based on the GM model and cannot be extrapolated to non-GM internal wave fields without additional numerical simulations. Polzin *et al.* (1995) suggest that non-GM *frequency* spectral shapes will have more impact on the relative roles of shear and vertical divergence than non-GM wavenumber spectral shapes.

3.3.2.3 Test-wave breaking. Figure 8 compares probability density functions (pdf) of background vertical divergence W_z (a), shear V_z (b) and strain ξ_z (c) at (i)

the instant test-wave vertical wavelengths fall below 5 m (solid), (ii) throughout the test-wave trajectories ($\lambda_z > 5$ m) (dotted), and (iii) randomly sampling the background fields [dashed, not in (d)]. That these three sets of curves are not identical points to strong correlations between the test waves and background overcoming the initial random phasing. Waves tend to “break” while encountering higher-than-average shear, vertical divergence and buoyancy frequency (solid curves, Fig. 8) as also reported from observations (Alford and Pinkel 1999). Prior to “breaking,” test waves experience lower-than-average shear, vertical divergence and buoyancy frequency (dotted, Fig. 8).

Taken together, Figs. 2–3 and 8 suggest the following wave/wave interaction scenario. While in lower-than-average shear and vertical divergence, test waves slowly migrate toward higher wavenumber (around $k_z = 0.05$ cpm) (1–2 h in Fig. 2). Upon encountering higher-than-average background shear, vertical divergence or strain, these finescale waves are rapidly forced toward even higher vertical wavenumber where they are assumed to break for $\lambda_z < 5$ m. Wave-induced variations in the vertical gradient of background buoyancy frequency are negligible. This scenario might also explain the change in spectral slope at $\lambda_z \sim 10$ m and the steeper finescale spectral slope for shear than strain.

4. Parameterizing the Turbulent Production Rate

Following Henyey *et al.* (1986), we ray-trace small-scale waves (referred to as test waves) in larger-scale Garrett and Munk (Munk 1981) internal-wave backgrounds (Appendices B and D, and Fig. 1) using (2.1)–(2.2).

It is not necessary to track individual test-wave amplitudes to estimate the spectral energy-flux by ray-tracing (Henyey *et al.* 1986; section 5). In order to parameterize the turbulence production rate $\varepsilon(1 + \gamma)$ using eikonal techniques, one quantifies the rate at which energy is fluxed toward high vertical wavenumber in the internal wave spectrum. Then the time rate of change of energy in the spectral interval $dk_z d\omega$ is

$$\frac{d\{S[E](k_z, \omega) dk_z d\omega\}}{dt} = S[E](k_z, \omega) \left\langle \frac{dk_z}{dt} \right\rangle d\omega + S[E](k_z, \omega) \frac{d\omega}{dt} dk_z, \quad (4.1)$$

assuming the energy density spectra $S[E](k_z, \omega)$ is invariant. The time rate of change of the vertical wavenumber $\langle dk_z/dt \rangle$ is a function of both vertical wavenumber k_z and intrinsic frequency ω . In a steady

state, the left-hand side of (4.1) vanishes. For an equilibrium spectrum, the second term of (4.1) vanishes so the first term of (4.1) can be equated to the turbulence production rate

$$\varepsilon - \langle w'b' \rangle = \varepsilon(1 + \gamma) = \int_f^N S[E](k_z, \omega) \left\langle \frac{dk_z}{dt} \right\rangle d\omega. \quad (4.2)$$

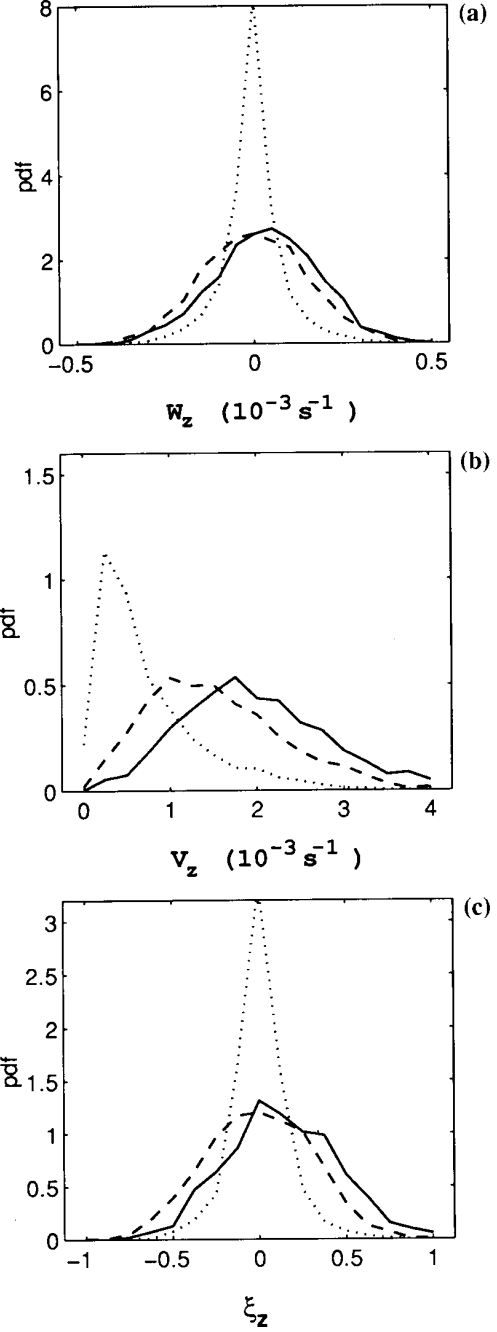


Figure 8. Comparison of probability density functions for background vertical divergence W_z (a), vertical shear V_z (b) and strain ξ_z (c) at sites where the test-wave vertical wave-

length λ_z falls below 5 m (solid), throughout the test-wave trajectories (dotted), and randomly sampling the background (dashed). Test-wave “breaking” ($\lambda_z < 5$ m) tends to occur at higher-than-average background shear, vertical divergence and buoyancy frequency (solid curves). Prior to “breaking” (dotted), test waves tend to propagate through lower-than-average shear, vertical divergence and buoyancy frequency.

4.1 Parameterizing Turbulent Production Rate With Both Shear and Vertical Divergence Variances

To include interactions with internal-wave vertical divergence W_z in the parameterization of the turbulence production rate $\epsilon(1 + \gamma)$ (4.2), the vertical wavenumber k_z ray-tracing equation (2.4) is used. The $(\partial\omega_i/\partial N_i)(\partial N_i/\partial z)$ term is negligible so will not be included here. Part of the high-frequency and high-horizontal-wavenumber vertical divergence term in dk_z/dt is reversible. In the following discussion, we first include the reversible part of dk_z/dt by estimating the ensemble time rate of change of the vertical wavenumber $\langle dk_z/dt \rangle$ in (4.2) from its rms value. This includes interactions with background waves that do not satisfy the WKB approximation. In section 4.2, we successively filter out reversible high-frequency and high-horizontal-wavenumber contributions to better satisfy WKB scale-separation.

First, following Henyey *et al.* (1986), we estimate $\langle dk_z/dt \rangle$ by its rms value

$$\begin{aligned} \left\langle \frac{dk_z}{dt} \right\rangle &\sim \sqrt{\left\langle \left(\frac{dk_z}{dt} \right)^2 \right\rangle} \\ &\sim r_1(k_z) k_z \sqrt{\langle V_z^2 \rangle} \left[\frac{k_h}{k_z} + r_2(k_z) \sqrt{\frac{\langle W_z^2 \rangle}{\langle V_z^2 \rangle}} \right] \\ &\sim r_1(k_z) k_z \sqrt{\langle V_z^2 \rangle} \left[\sqrt{\frac{\omega^2 - f^2}{N^2 - \omega^2}} + r_2(k_z) \sqrt{\frac{\langle W_z^2 \rangle}{\langle V_z^2 \rangle}} \right] \end{aligned} \quad (4.3)$$

where functions $r_1(k_z)$ and $r_2(k_z)$ indicate correlations between test waves and background. It has been assumed that the shear and vertical divergence terms are uncorrelated. Including vertical divergence in the ray-tracing equation augments the shear-only $\langle dk_z/dt \rangle$ with the term involving the ratio of the rms vertical divergence to rms shear $\sqrt{\langle W_z^2 \rangle / \langle V_z^2 \rangle}$.

Following Henyey *et al.* (1986), the spectral density $S[E](k_z, \omega)$ is described by the Munk (1981) GM model (with an additional k_z^{-1} dependence for wavenumbers

$k_z > k_{zc} \approx 0.08$ cpm to simulate the finescale oceanic spectra, Gargett *et al.* 1981; Gregg *et al.* 1993)

$$S[E](\omega, k_z) = \frac{4fN^2 b j_* E_{GM}}{\pi} \frac{1}{\omega \sqrt{\omega^2 - f^2}} \frac{k_{zc}}{k_z^3}. \quad (4.4)$$

GM model parameters are defined in Table 1. Substituting $\langle dk_z/dt \rangle$ from (4.3) and $S[E](\omega, k_z)$ from (4.4) into (4.2),

$$\begin{aligned} \epsilon_1(1 + \gamma) &= \frac{12 Ri_c f N^2 b^2 j_*^2 E_{GM}^2}{\pi} \\ &\times \left(\frac{k_{zc}}{k_z} \right)^2 r_1(k_z) \frac{\sqrt{\langle V_z^2 \rangle}}{N} \\ &\times \left[\text{I} \text{ Arccosh} \left(\frac{N}{f} \right) + r_2(k_z) \frac{N}{f} \text{ Arccos} \left(\frac{f}{N} \right) \sqrt{\frac{\langle W_z^2 \rangle}{\langle V_z^2 \rangle}} \right] \end{aligned} \quad (4.5)$$

expressed in terms of the internal-wave shear variance $\langle V_z^2 \rangle$ (I) and vertical divergence variance $\langle W_z^2 \rangle$ (II). Ignoring the vertical divergence term (II) reproduces Henyey *et al.*'s (1986) shear-based model, where $\sqrt{\langle V_z^2 \rangle} / N^2$ is equivalent to their $\langle Ri \rangle^{-1/2} = Ri_c^{-1/2} [1 + \ln(k_z/k_{zc})]^{1/2}$. Correlation $r_1(k_z)$ between test-wave vertical wavenumber and background shear is equivalent to their constant ratio $(1-r)/[\sqrt{2}(1+r)]$ related to the ratio of up- and down-wavenumber spectral energy-flux in k_z -space. In GM, the relationship between the wavenumber of the finescale change in spectral slope k_{zc} and the associated Richardson number Ri_c is $Ri_c^{-1} = 3j_* b k_{zc} E_{GM}$ (Munk 1981; Henyey *et al.* 1986).

The spectral energy-flux toward high wavenumber $\epsilon(1 + \gamma)$ is independent of k_z for the GM model spectrum, as will be verified with numerical simulations (see Fig. 11 in Sec. 5.2); otherwise, energy would accumulate or deplete from intermediate wavenumbers. This eliminates the k_z dependence in (4.5)

$$\begin{aligned} \epsilon_1(1 + \gamma) &= \frac{12 Ri_c b^2 j_*^2 f N^2 E_{GM}^2}{\pi} \\ &\times \left(\frac{k_{zc}}{0.2\pi \text{ rad m}^{-1}} \right)^2 r_1 \frac{\sqrt{\langle V_z^2 \rangle}}{N} \\ &\times \left[\text{I} \text{ Arccosh} \left(\frac{N}{f} \right) + r_2 \frac{N}{f} \text{ Arccos} \left(\frac{f}{N} \right) \sqrt{\frac{\langle W_z^2 \rangle}{\langle V_z^2 \rangle}} \right] \Big|_{k_z=0.2\pi \text{ rad m}^{-1}} \end{aligned} \quad (4.6)$$

where correlation coefficients $r_1 = 0.022$ and $r_2 = 1.7$ for the upper limit ($K_z < k_z$, no restriction on background horizontal wavenumber and frequency) are determined numerically (see dotted line in Fig. 10, Sec. 5.2). For the Munk (1981) model spectrum, the total rms ratio

$$\sqrt{\frac{\langle (W_z)^2 \rangle}{\langle (V_z)^2 \rangle}} = \sqrt{\frac{\int_f^N \mathcal{S}[W_z](\Omega) d\Omega}{\int_f^N \mathcal{S}[V_z](\Omega) d\Omega}} = \sqrt{\frac{4f}{3\pi N}}. \quad (4.7)$$

Equation (4.7) indicates that (II)/(I) is proportional \sqrt{N} , that is, the contribution from vertical divergence has a 0.5 stronger dependence on N than the shear. This extra \sqrt{N} scaling in (II) arises from the contribution of near-buoyancy frequency waves in the GM spectra to the vertical divergence W_z . It is not consistent with the N^2 dependence in observations (Polzin *et al.* 1995).

Because near-buoyancy background wave periods are much shorter than test-wave lifespans, and their horizontal wavenumbers much higher than those of fine-scale near-inertial test waves, including their rms variance will overestimate the spectral energy transfer. That is, the upper bound (4.6) with the given correlation coefficients is not realistic. These simulations include waves that do not satisfy WKB scale-separation in time or the horizontal. In section 4.2, we examine the effect of averaging vertical divergence over test-wave lifespans and applying WKB scale-separation in the horizontal. This leads to a parameterization in terms of shear and strain variances.

4.2 Parameterizing Turbulent Production Rate With Shear and Strain Variances

As mentioned in section 4.1, there is concern about parameterizing $\langle dk_z/dt \rangle$ and $\epsilon(1 + \gamma)$ in terms of the rms variance of vertical divergence $\langle W_z^2 \rangle$ in (4.5) and (4.6) because vertical divergence is dominated by near-buoyancy waves of short time- and horizontal length-scales that do not satisfy the WKB approximation. Near-buoyancy waves dominate the rms $k_z W_z$, but not the test-wave lifespan average $\langle k_z W_z \rangle$ if high-frequency variations are reversible. Therefore, estimating $\langle dk_z/dt \rangle$ by the rms variance $k_z W_z$ exaggerates the role of high-frequency waves in spectral energy transfer.

To filter out high-frequency fluctuations which do not contribute to the ensemble average $\langle dk_z/dt \rangle$, we first estimate $\langle dk_z/dt \rangle$ from the ensemble average changes in test-wave vertical wavenumber Δk_z over the lifespans of the test waves Δt , that is,

$$\left\langle \frac{dk_z}{dt} \right\rangle \simeq \left\langle \frac{\Delta k_z}{\Delta t} \right\rangle = \left\langle \frac{1}{\Delta t} \int_0^{\Delta t} \frac{dk_z}{dt} dt \right\rangle, \quad (4.8)$$

and later impose horizontal scale-separation. Test-wave lifespans (while wavelength $\lambda_z > 5$ m) in the numerical simulations vary from of order an hour at the base of the mixed-layer to tens of hours at 2000-m depth. During the lifespan of test waves, test-wave wavenumbers k_h, k_z and encountered background vertical shear V_z vary much more slowly than background vertical divergence W_z . Thus, the influence of high-frequency ($> 2\pi/\Delta t$) internal waves is filtered out in (4.8). We estimate

$$\left\langle \int_0^{\Delta t} (dk_z/dt) dt / \Delta t \right\rangle$$

by the rms

$$\left\{ \int_0^{\Delta t} (dk_z/dt) dt \right\} / \Delta t$$

To zero order,

$$\begin{aligned} \left\langle \frac{dk_z}{dt} \right\rangle &\simeq \text{rms } k_h \cdot V_z + \text{rms } \frac{k_z \xi_z}{\Delta t} \\ &= \sqrt{\langle (k_z V_z)^2 \rangle} \left[\frac{k_h}{k_z} + \frac{1}{\Delta t} \sqrt{\frac{\langle \xi_z^2 \rangle}{\langle V_z^2 \rangle}} \right] \end{aligned} \quad (4.9)$$

$$= r_1(k_z) k_z \sqrt{\langle V_z^2 \rangle} \left[\sqrt{\frac{\omega^2 - f^2}{N^2 - \omega^2}} + r_2(k_z) \sqrt{\frac{f^2 \langle \xi_z^2 \rangle}{\langle V_z^2 \rangle}} \right]$$

where $r_2(k_z)$ is related to the ratio of the test-wave lifetime Δt to the inertial timescale f^{-1} as well as the correlation between test-wave vertical wavenumber and background vertical strain.

As in Polzin *et al.* (1995), it is assumed that the turbulence production rate can be parameterized in terms of internal-wave shear $\langle V_z^2 \rangle$ and strain $\langle \xi_z^2 \rangle$ variances. With $\langle dk_z/dt \rangle_E$ from (4.9), the turbulence production rate (4.2) independent of k_z is given by

$$\begin{aligned}
\varepsilon_2(1 + \gamma) &= \frac{12 Ri_c b^2 j^{*2} f N^2 E_{GM}^2}{\pi} \\
&\times \left(\frac{k_{zc}}{0.2\pi \text{ radm}^{-1}} \right)^2 r_1 \cdot \frac{\sqrt{\langle V_z^2 \rangle}}{N} \\
&\times \left[\text{Arccosh} \left(\frac{N}{f} \right) + r_2 \cdot \text{Arccos} \left(\frac{f}{N} \right) \sqrt{\frac{N^2 \langle \zeta_z^2 \rangle}{\langle V_z^2 \rangle}} \right]
\end{aligned} \tag{4.10}$$

where $\langle V_z^2 \rangle / (\bar{N}^2 \langle \zeta_z^2 \rangle)$ ($= 3$ in GM) is the shear-to-strain ratio, and correlation coefficients $r_1 = 0.22$ and $r_2 = 25$ are determined numerically by carrying out simulations with and without interactions with vertical divergence as in (4.6).

No frequency or horizontal wavenumber filtering were applied to the numerical simulations to obtain the r_1 and r_2 correlation coefficients for ε_2 so these represent another

upper limit for turbulence production; indeed, the numerical simulations to obtain the upper limit of (4.10) were identical to those for (4.6). A lower limit ε_2 is obtained by applying stricter vertical scale-separation $K_z < 0.5k_z$ and horizontal scale-separation $K_H < k_h$ for frequencies

$\Omega > 11f$. This yields correlation coefficients $r_1 = 0.01$ and $r_2 = 10$ in (4.10). The upper and lower limits of (4.10) differ by a factor of four.

Parameterizing $\varepsilon(1 + \gamma)$ with shear and strain variances (4.10) predicts an N^2 scaling, consistent with the predicted scalings of Henyey *et al.* (1986) and weak-triad interactions (McComas and Müller 1981b), and observations (Polzin *et al.* 1995). Replacing vertical divergence by the test-wave time-averaged change in strain filters out the high-frequency contributions to vertical divergence which produced a stronger dependence on N in (4.6). Thus, we suggest that the lower limit of (4.10) is a more reasonable parameterization. It averages over test-wave lifespans and better satisfies the WKB approximation and observations. However, although (4.10) is expressed in terms of strain, it should be emphasized that *physically* it is vertical divergence that induces internal-wave spectral energy transfer.

Table 2. Correlation coefficients for turbulence production rate parameterizations (4.6) and (4.10) based on numerical ray-tracing simulations with various assumptions.

Model Assumptions	r_1	r_2
1. (4.6) $V_z, W_z (K_z < k_z)$	0.022	1.7
2. (4.10) $V_z (K_z < k_z)$	0.022	0
3. (4.10) $V_z (K_z < 0.5k_z)$ $K_H < k_h$ (or $\Omega < 11f$)	0.010	0
4. (4.10) $V_z, \zeta_z (K_z < k_z)$	0.022	25
5. (4.10) $V_z, \zeta_z (K_z < 0.5k_z)$ $K_H < k_h$ (or $\Omega < 11f$)	0.010	10
	c_I	r_2
6. (6.1) $V_z, \zeta_z (K_z < k_z)$	1.0×10^{-8}	25
7. (6.1) $V_z, \zeta_z (K_z < 0.5k_z)$ $K_H < k_h$ (or $\Omega < 11f$)	0.4×10^{-8}	10

4.3 Summary

Several parameterizations for the turbulent production rate $\varepsilon(1 + \gamma)$ have been presented (Table 2). Equation (4.6) parameterizes the turbulent production rate in

terms of the total internal-wave vertical divergence $\langle W_z^2 \rangle$ and vertical shear $\langle V_z^2 \rangle$ variances so represents an upper limit. The problem with this parameterization is that it expresses test-wave lifespan average $\langle dk_z/dt \rangle$ in terms of the total vertical divergence variance which contains significant contributions from wave periods shorter than test-wave lifespans and horizontal wavelengths smaller than those of the test waves, in violation of the WKB approximation. To overcome this failing, equation (4.10) parameterizes $\varepsilon(1 + \gamma)$ with the vertical strain $N^2 \langle \xi_z^2 \rangle$ and vertical shear $\langle V_z^2 \rangle$ variances by filtering out the reversible high-frequency parts of vertical divergence in dk_z/dt . An upper limit from (4.10) is obtained from the same numerical simulations used to estimate the correlation coefficients in (4.6), that is, by applying scale-separation only in the vertical ($K_z < k_z$). A lower limit is obtained by applying stricter scale-separation in the vertical ($K_z < 0.5k_z$) and scale-separation in the horizontal ($K_H < k_h$) for frequencies $\Omega > 11f$. Applying horizontal scale-separation $K_H < k_h$ at all background frequencies, or frequency scale-separation $\Omega < \omega$, causes many test waves to get stuck at low horizontal wavenumber and low frequency with no background to interact with. This is not realistic. Placing no horizontal restrictions on backgrounds with $\Omega < 11f$ is a compromise which allows test waves to interact with 95% of the shear and 90% of the strain. Observations lie between the upper and lower limits of (4.10) (see Fig. 14b in Sec. 6), roughly consistent with measurement uncertainty.

5. Numerically Simulating the Spectral Energy Transfer

Following Henyey *et al.* (1986), we calculate the GM spectral energy transfer (assumed equal to the turbulence production rate, $\varepsilon_p = \varepsilon + \langle w' b' \rangle$). In a steady state, the spectral energy transfer rate through a fixed vertical wavenumber can be expressed by the energy transfer rate following vertical wavenumber changes of the wavepackets. Procedure details follow.

From the ocean surface to 2000-m depth, 20 test-wave trajectories are released every 200 m in depth with fixed initial horizontal wavenumbers $(k_x, k_y) = (10^{-3} \text{ cpm}, 0)$ and vertical wavenumbers ranging from $k_z = -0.1$ to 0.1 cpm ($k_z \neq 0$) in steps of $\Delta k_{z0} = 0.01 \text{ cpm}$, corresponding to vertical wavelengths $\lambda_z = 10\text{--}100 \text{ m}$. Test waves are released in Monte Carlo background internal-wave fields described by the Garrett and Munk model spectrum (Munk 1981) in an exponential mean buoyancy frequency profile ranging from $4.9 \times 10^{-3} \text{ rad s}^{-1}$ at 100-m depth to $1.1 \times 10^{-3} \text{ rad s}^{-1}$ at 2000-m depth (Table 1). When test-wave vertical wavelengths fall below $\lambda_z = 5 \text{ m}$ ($k_z \geq 0.2 \text{ cpm}$), they are defined to

“break” and lose their energy to turbulence. At this wavenumber, stability parameters, such as Richardson number and instantaneous buoyancy, approach criticality in the ocean (Munk 1981; Müller *et al.* 1986; Polzin 1996). A total of 4000 test waves are propagated in 20 different Monte Carlo simulations of a GM background (Fig. 1) to obtain stable ensemble averages that span all phases of the initial background wave field.

To calculate the spectral energy-flux toward high wavenumber k_z in the high-wavenumber domain ($0.01 \text{ cpm} < k_z < 0.2 \text{ cpm}$, $k_h > 10^{-3} \text{ cpm}$), we assign an initial spectral action-flux into this spectral domain at the fixed initial horizontal wavenumber $k_{h0} = 10^{-3} \text{ cpm}$. This initial spectral action-flux will be redistributed by smallscale test wavepackets in phase space. How much action should be initially assigned to each test wave is determined by $q \cdot S[A](k_{h0}, k_{z0}) \cdot \Delta k_{z0} \cdot dk_{h0}/dt|_{t=0}$, where $S[A](k_h, k_z)$ is the GM action spectrum in terms of horizontal and vertical wavenumber, dk_{h0}/dt the initial horizontal wavenumber flux (to be discussed later), q a constant chosen such that the sum over all the test waves has the same total action as the high-wavenumber part of GM spectra

$$q \sum_{i=1}^{NW} S[A](k_{h0}, k_{z0}) \Delta k_{z0} \frac{dk_{h0}}{dt} \Big|_{t=0} \cdot \Delta t_i \quad (5.1)$$

$$= \int_{k_{h0}}^{\infty} \int_{k_{z\text{low}}}^{k_{zb}} S[A](k_h, k_z) dk_z dk_h,$$

NW the number of test waves, Δt_i the lifetime of the i th test wave, $k_{z\text{low}} = 0.01 \text{ cpm}$ is the lowest and $k_{zb} = 0.2 \text{ cpm}$ the highest (final or “breaking”) test-wave vertical wavenumbers.

Since the spectral action-flux $S[A](k_{h0}, k_{z0}) \Delta k_{z0} dk_{h0}/dt|_{t=0}$ is conserved following a test wave (Lighthill 1978), the spectral energy transfer rate through $k_z = 0.2 \text{ cpm}$ (\equiv turbulence production rate) can be calculated from the spectral action-flux multiplied by the intrinsic frequencies of the test waves as they break ($k_z \geq k_{zb}$), that is,

$$\varepsilon(1 + \gamma) = q \sum_{i=1}^{NW} \left\{ S[A](k_{h0}, k_{z0}) \Delta k_{z0} \frac{dk_{h0}}{dt} \Big|_{t=0} \right\} \omega_{bj} \quad (5.2)$$

where ω_{bj} is the j th test-wave breaking frequency, ε the turbulent kinetic energy dissipation rate and $\gamma = -\langle w' b' \rangle / \varepsilon \leq 0.2$ the mixing efficiency.

Three approaches are used to select the initial horizontal wavenumber flux rate $dk_{h0}/dt|_{t=0}$ for (5.2):

- for the shear and vertical divergence parameterization (4.6), evaluating the rms horizontal wavenumber ray-tracing equation

$$\frac{dk_{h_0}}{dt} \Big|_{t=0} \sim k_{h_0} \sqrt{\langle (\nabla_h V_h)^2 \rangle} + k_{z_0} \sqrt{\langle (\nabla_h W)^2 \rangle}, \quad (5.3)$$

where $\sqrt{\langle (\nabla_h V_h)^2 \rangle}$ and $\sqrt{\langle (\nabla_h W)^2 \rangle}$ are calculated from GM model spectrum (Munk 1981), but with an extra factor $(N^2 - \omega^2)/(N^2 - f^2)$ in $S[W](\omega, k_z)$ to be consistent with the nonhydrostatic internal-wave equations of motion.

- for shear-and-strain parameterization (4.10), test-wave lifespan-averaged dk_{h_0}/dt is evaluated, that is,

$$\begin{aligned} \frac{dk_{h_0}}{dt} \Big|_{t=0} &\sim \text{rms} \left\{ \frac{1}{\langle \Delta t \rangle} \int_0^{\Delta t} \frac{dk_h}{dt} dt \right\} \\ &\sim k_{h_0} \sqrt{\langle (\nabla_h V_h)^2 \rangle} + \frac{k_{z_0}}{\langle \Delta t \rangle} \sqrt{\langle (\nabla_h \xi)^2 \rangle}, \end{aligned} \quad (5.4)$$

where $\langle \Delta t \rangle$ is the ensemble-averaged lifespan of the test waves. In this case, $dk_{h_0}/dt|_{t=0}$ is independent of N . The distinction between (5.3) and (5.4) was discussed in connection with (4.6) and (4.10).

- constant so that $dk_{h_0}/dt|_{t=0}$ is independent of both test-wave initial wavenumber and background buoyancy frequency N . (5.5)

Numerically-simulated test-wave vertical wavenumber spectral shapes for action (Fig. 9) prove insensitive to the choice of initial conditions (5.3–5.5). Because of the normalization q in (5.1) and (5.2), the simulated $\epsilon(1 + \gamma)$ are independent of the magnitude of $dk_{h_0}/dt|_{t=0}$ (Fig. 10). However, whether the calculated $\epsilon(1 + \gamma)$ varies as $N^{2.5}$ or N^2 (Fig. 10) depends on how $dk_{h_0}/dt|_{t=0}$ varies with N [as \sqrt{N} for (5.3), or independent of N for (5.4) and (5.5)]. In the following, numerical results are ensemble-averaged over all backgrounds and trajectories.

5.1 The High-Wavenumber Spectra

Figure 9 displays numerically-simulated test-wave vertical wavenumber spectra for action $S[A](k_z)$ normalized by GM at vertical wavenumbers $0.01 \text{ cpm} < k_z < k_{z_b} = 0.2 \text{ cpm}$ ($100 \text{ m} > \lambda_z > 5 \text{ m}$) for vertical scale-separation $K_z < k_z$ and horizontal scale-separation $K_H < k_h$ for $\Omega > 11f$. When interactions with both shear and vertical divergence are included, the spectral slope is $k_z^{-1/2}$ steeper than GM (k_z^{-2}) below the finescale cutoff wavenumber $k_{z_c} = 0.08 \text{ cpm}$. In the absence of vertical divergence interactions, the wavenumber spectral slope is the same as the GM model. These results are consistent with weak-triad interaction theory. McComas and Müller (1981a) argued that, to maintain a spectral action transfer independent of vertical wavenumber, re-

quires a $k_z^{-2.5}$ dependence at low frequencies ($\omega_i < 4f$) and a k_z^{-2} dependence at high frequencies ($\omega_i > 5f$)—where interactions with vertical shear control the spectral action transfer. Since the ω^{-3} action spectra is dominated by low-frequency waves, it should display a $k_z^{-2.5}$ dependence. A $k_z^{-2.5}$ high-wavenumber ($0.01 \text{ cpm} < k_z < 0.1 \text{ cpm}$) energy spectra was observed by Leaman and Sanford (1975) and Pinkel (1984) but is less discernible in other observations (e.g., Gregg *et al.* 1993; Polzin *et al.* 1995). Whether ocean spectra behave as $k_z^{-2.5}$ or k_z^{-2} may depend on the strength of interactions with the high-frequency wave field.

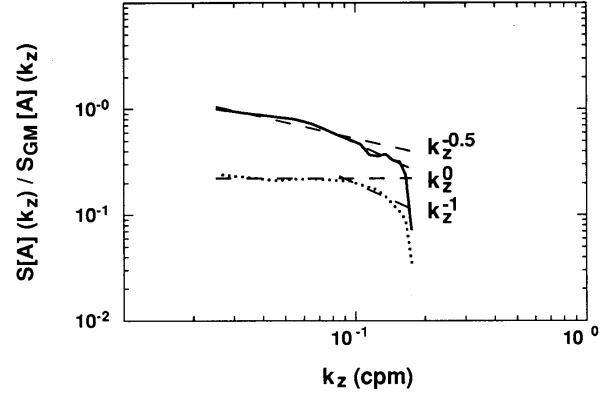


Figure 9. Vertical wavenumber spectra for test-wave action normalized by the GM model spectrum. Solid (dotted) curves include (exclude) vertical divergence $k_z W_z$ interactions. Dashed lines indicate labeled k_z power laws. Magnitudes of the two test-wave action spectra have been arbitrarily shifted vertically to make the plot clearer. With vertical divergence $k_z W_z$ interactions, the vertical wavenumber spectra is $k_z^{-0.5}$ steeper than GM at low wavenumbers ($0.01 \text{ cpm} < k_z < 0.08 \text{ cpm}$), consistent with weak-triad theory. At wavenumbers $k_z > 0.08 \text{ cpm}$ ($\lambda_z < 12 \text{ m}$), test-wave spectral slopes are k_z^{-1} steeper than at lower wavenumbers, that is, have a k_z^{-3} dependence, consistent with observed finescale spectra.

The GM-normalized test-wave action spectra steepen at finescale wavenumbers above $k_{z_c} = 0.08 \text{ cpm}$ ($\lambda_z = 12 \text{ m}$; Fig. 9) whether interactions with background vertical divergence are included or not. The high-wavenumber test-wave spectra are k_z^{-1} steeper than the low-wavenumber GM spectra, that is, finescale action spectra have a k_z^{-3} dependence, consistent with observed finescale spectra (Gargett *et al.* 1981; Gregg *et al.* 1993). The change in spectral slope can be interpreted as arising from strong interactions between test waves and the background when test waves reach high wavenumbers and come in direct contact with the breaking wavenumber sink (Hines 1991; Fig. 3).

5.2 Simulated Turbulence Production Rates $\epsilon(1 + \gamma)$

Figure 10 displays profiles of the turbulence production rate $\epsilon(1 + \gamma)$ under various filtering assumptions. Coefficients r_1 and r_2 for the different assumptions are listed in Table 2. Upper limits for the shear-and-strain predictions are consistent with weak-triad results (McComas and Müller 1981b). However, both weak-triad and ray-tracing approaches are in violation of their assumptions in this limit.

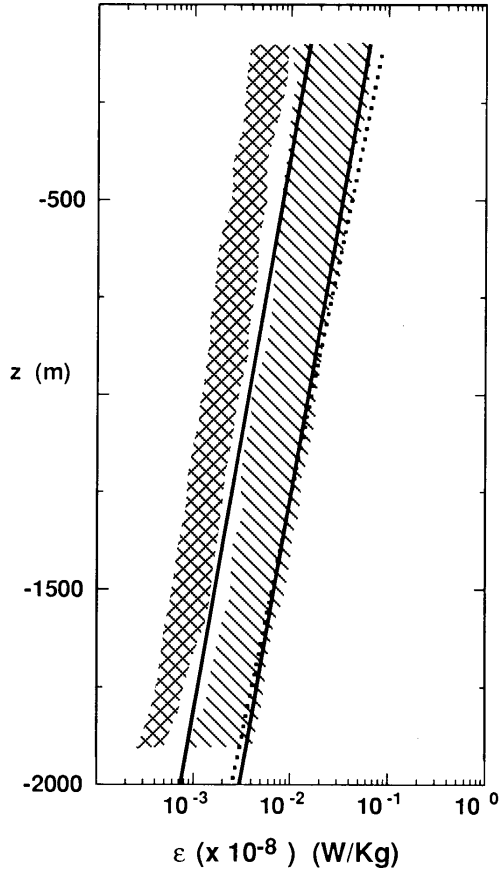


Figure 10. Profiles of predicted turbulent dissipation rate ϵ [converted from turbulent production rate $\epsilon(1 + \gamma)$ using $\gamma = 0.2$] in stratification $N(z) = N_0 e^{z/b}$ (Table 1). Crosshatching spans the upper and lower limits of shear-only simulations, stippling the upper and lower limits of shear-and-strain simulations. Upper limits include all interactions satisfying $K_z < k_z$, lower limits restrict $K_H < k_h$ for $\Omega > 11f$ and $K_z < 0.5k_z$. The dotted curve is parameterization (4.6) in terms of shear and vertical divergence, the right solid curve the shear-and-strain upper limit of (4.10), and the left solid curve the shear-only upper limit of (4.10). The upper limit of the predicted shear-and-strain ϵ is close to the weak-triad result (McComas and Müller 1981b) and 3–4 times the shear-only upper limit (Heney *et al.* 1986). The lower limit of the predicted shear-and-strain ϵ is close to the shear-only upper limit (Heney *et al.* 1986).

Applying WKB scale-separation to horizontal wavenumbers $K_H < k_h$ for $\Omega > 11f$, and more strictly to vertical wavenumber $K_z < 0.5k_z$, reduces shear-and-strain turbulence production rates by a factor of four and shear-only predictions by a factor of two. Turbulence production rate estimates with $K_z < 0.5K_z$ are a third those with $K_z < k_z$ (see Fig. 12 in Sec. 5.3), so horizontal scale-separation accounts for the remaining difference. The lower-limit shear-and-strain values are consistent with upper-limit shear-only predictions (Heney *et al.* 1986) and therefore observations (Gregg 1989; Polzin *et al.* 1995).

The simulated spectral energy transfer is not sensitive to the magnitude of the initial $dk_{h0}/dt|_{t=0}$ [because of normalizing factor q in (5.1)], initial test-wave wavenumber or initial frequency. But the buoyancy frequency scaling of $\epsilon(1 + \gamma)$ is sensitive to the N dependence of $dk_{h0}/dt|_{t=0}$ (Fig. 10). The test-wave lifespan-averaged or constant $dk_{h0}/dt|_{t=0}$ in both (5.4) and (5.5) are independent of N and give the same numerically calculated $\epsilon(1 + \gamma)$ with N^2 scaling (4.10). But the rms $dk_{h0}/dt|_{t=0}$ in (5.3) has a \sqrt{N} dependence, due to $\sqrt{\langle (\nabla_h W)^2 \rangle}$ being dominated by near-buoyancy waves in the GM model, and results in an $N^{2.5}$ dependence in the numerically-calculated $\epsilon(1 + \gamma)$ (4.6) which is not consistent with the observed N^2 dependence (Polzin *et al.* 1995).

We speculate that the lower limit of parameterization (4.10), expressed in terms of shear and lifespan-averaged vertical divergence, that is, strain, is the more reasonable choice since instantaneous high-frequency high-horizontal-wavenumber vertical divergence fluctuations do not necessarily contribute to the net spectral energy transfer. The lower limit is also more consistent with the WKB approximation and most of the observations (see Fig. 14). These speculations await further observational or numerical testing.

The numerically-calculated spectral energy transfer is independent of the breaking wavenumber k_{zb} (Fig. 11). Therefore, the GM vertical wavenumber spectra is in equilibrium with respect to ray-tracing wave/wave interactions at high wavenumber, consistent with our assumptions. Figures 4 and 5 suggest that the finescale equilibrium frequency spectra has a gentler spectral slope than GM.

5.3 Sensitivity to Vertical Scale-Separation

The WKB approximation, and the requirement that test waves not modify the background during interactions, are two crucial assumptions for ray-tracing wave/wave interactions. Their validity requires scale-separation ($\lambda < \Lambda$) between test waves and background.

The degree of scale-separation required is uncertain. In particular, our simulations show a strong contribution for waves with $\lambda \sim \Lambda$ which may not satisfy WKB scale-separation.

Figures 12 and 13 examine the sensitivity of upper-limit spectral energy transfer rates to different vertical scale-separations between test waves and background. When vertical wavenumbers of the background are restricted merely to be lower than those of the test waves ($K_z < k_z$, $\max K_z = k_z$, solid), the simulated turbulence production $\epsilon(1 + \gamma)$ is 1.6 times greater than when background vertical wavenumbers are restricted to be at most half ($K_z < 0.5k_z$, dotted), and 4.7 times greater than when background vertical wavenumbers are at most a fifth the test waves' ($K_z < 0.2k_z$, dashed). These results are independent of buoyancy frequency (Fig. 13). Since the background shear and vertical

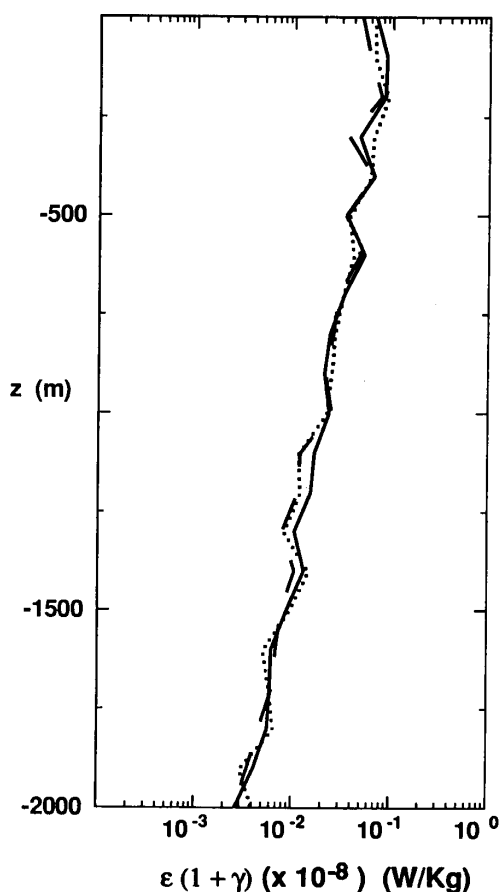


Figure 11. Numerically-simulated spectral energy transfer rate $\epsilon(1 + \gamma)$ profiles for different test-wave breaking wavenumbers, $k_z = 0.1$ cpm (solid), $k_z = 0.2$ cpm (dotted) and $k_z = 0.5$ cpm (dashed). Energy transfer rates, and their dependence on buoyancy frequency N , are independent of the assumed test-wave breaking vertical wavenumber.

divergence variances $\int_0^{\max K_z} S(k_z)dk_z$ are proportional to $\max K_z$. Figs. 12 and 13 indicate that the spectral energy transfer rate is slightly less sensitive to variance at higher wavenumbers than lower wavenumbers. That is, interactions between waves of similar scale partially cancel on average. This implies that the turbulence production rate might be sensitive to the wavenumber-content of the wave field as well as the frequency-content (discussed in section 4, see also Polzin *et al.* 1995). This raises doubts about finescale parameterizations such as (4.6) and (4.10) which do not take into account which vertical wavenumbers contribute to shear and strain variances. Further work is needed to quantify these uncertainties.

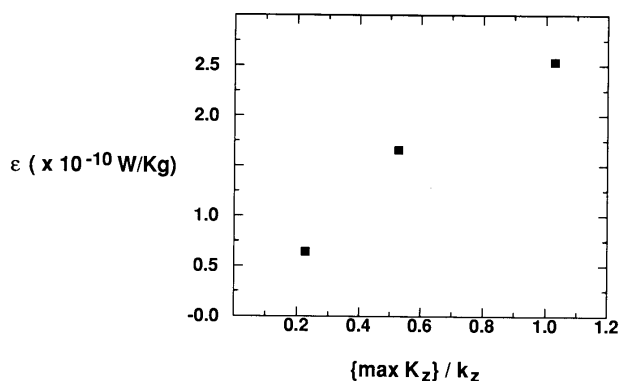


Figure 12. Numerically-simulated depth-averaged energy transfer rates $\epsilon(1 + \gamma)$ as a function of imposed separation between background and test-wave vertical wavenumbers $\{\max K_z\}/k_z$. For a greater degree of vertical scale-separation, the simulated energy transfer rate drops off. The calculated ϵ when $K_z < k_z$ is a factor of 1.6 greater than when $K_z < 0.5k_z$, and 4.6 times greater than when $K_z < 0.2k_z$. Because the variances in the GM spectra are proportional to $\max K_z$, the horizontal axis can be thought of as background shear or strain variance. Thus, energy transfer rates are slightly less sensitive to background variance at higher wavenumbers K_z .

As discussed by Henyey (1984), a factor-of-two separation in vertical wavenumbers might be sufficient to ensure (i) validity of the WKB approximation and (ii) the assumption that the background is not altered by wave/wave interactions. However, interactions between waves with less than a factor-of-two scale-separation contribute significantly (a third) to the ray-tracing spectral energy transfer rate (Figs. 12 and 13). In Henyey *et al.* (1986) and the upper-limit numerical simulations presented here, vertical wavenumbers of the background are merely restricted to be lower than those of the test waves ($K_z < k_z$), so the calculated $\epsilon(1 + \gamma)$ in Fig. 10 includes all such interactions. Figure 12 can be interpreted as implying that one third of the upper-limit

ray-tracing spectral energy transfer is associated with waves that are not strictly WKB scale-separated in the vertical ($K_z > 0.5k_z$). Whether oceanic interactions are stronger or weaker than WKB for these waves is unknown.

5.4 Sensitivity to Horizontal Scale-Separation

Applying WKB horizontal scale-separation ($K_H < k_h$) as well as stricter vertical scale-separation ($K_z < 0.5k_z$) reduces the shear-and-strain predictions by a factor of four (2/3 due to horizontal and 1/3 due to vertical scale-separation) and the shear-only predictions by a factor of two compared to simulations that allow interactions with background waves of all horizontal wavenumbers. This suggests that, even for shear-only calculations, the issue of horizontal scale-separation cannot be ignored as was done by Henyey *et al.* (1986) and Polzin *et al.* (1995).

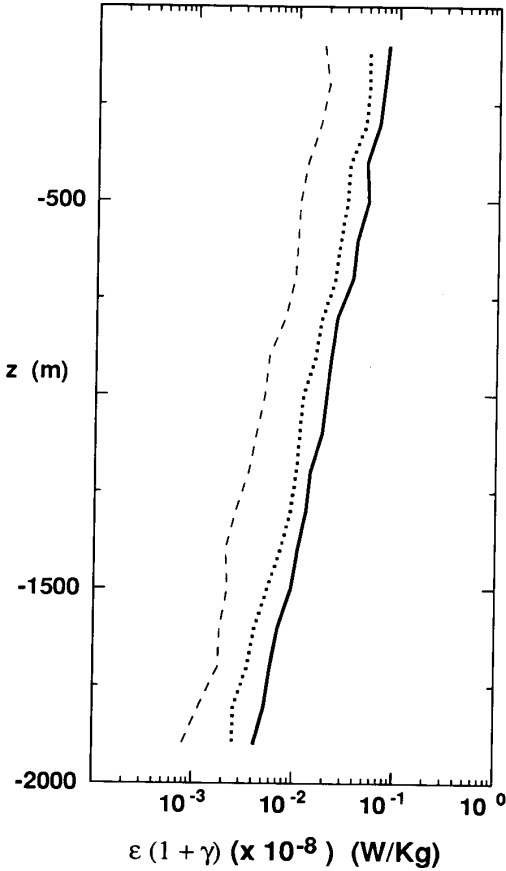


Figure 13. Numerically-simulated spectral energy transfer rate $\varepsilon(1 + \gamma)$ profiles when background vertical wavenumbers K_z are restricted to be lower ($K_z < k_z$; solid), no more than half ($K_z < 0.5k_z$; dotted) and no more than one fifth ($K_z < 0.2k_z$; dashed) those of the test waves. The dependence on

buoyancy frequency N is independent of the degree of vertical scale-separation.

6. Can GM-based Models be Simplified and Extended to non-GM?

Parameterizations (4.6) and (4.10) are convenient for comparison with Henyey *et al.*'s (1986) GM-based model (1.4), but not oceanic observations because: (i) model parameters such as Ri_c , j^* , E_{GM} and k_{zc} can be difficult to estimate from observations, are not independent (Munk 1981; Duda and Cox 1989; Smith *et al.* 1987) and are not fundamental controlling dynamical variables, and (ii) oceanic internal wave fields deviate from GM. To apply the model to the range of internal wave fields observed in the ocean, Gregg (1989), Wijesekera *et al.* (1993) and Polzin *et al.* (1995) re-expressed Henyey *et al.*'s (1986) GM model in terms of either shear variance, strain variance or both, then compared them to nearly GM and non-GM observations. We will refer to these rewritten parameterizations as *extended models*.

In this section, we formulate and compare extended parameterizations with each other and the observations of Polzin *et al.* (1995). Some of the difficulties in applying these models to the real ocean will be revealed in the process. We express the GM-based parameterizations (4.10) with shear and strain variances to facilitate comparison with Gregg (1989), Wijesekera *et al.* (1993) and Polzin *et al.* (1995).

Variances of shear $\langle V_z^2 \rangle$ and vertical strain $\langle \xi_z^2 \rangle$ are substituted for the GM model parameters j^* , E_{GM} and k_{zc} in (4.10) using GM model relations to yield

$$\varepsilon(1 + \gamma) = c_1 f N^2 b^2 \left[1 + \frac{N^2 \langle \xi_z^2 \rangle}{\langle V_z^2 \rangle} \right]^2 \left(\frac{\sqrt{\langle V_z^2 \rangle}}{N} \right)^4 \times \left[\text{Arccosh} \left(\frac{N}{f} \right) + r_2 \text{Arccos} \left(\frac{f}{N} \right) \sqrt{\frac{N^2 \langle \xi_z^2 \rangle}{\langle V_z^2 \rangle}} \right] \quad (6.1)$$

where $\sqrt{\langle V_z^2 \rangle}/N = 0.7$ and $\langle V_z^2 \rangle/(N^2 \langle \xi_z^2 \rangle) = 3$ in the GM model (Munk 1981). We choose shear and strain variances because they appear as fundamental physical parameters in the test-wave lifespan-averaged vertical ray-tracing equation and are readily measured. Doing so eliminates dependence on large-scale quantities j^* and E . We have replaced the $\sqrt{\langle V_z^2 \rangle}/N$ in (4.10) arising from dk_z/dt with $Ri_c^{-1/2} [1 + \ln(k_z/k_{zc})]^{1/2}$, where $Ri_c = 2$ and $k_z/k_{zc} = 2$, consistent with Henyey *et al.* (1986). If it

were retained, (6.1) would depend on $(\sqrt{\langle V_z^2 \rangle} / N)^5$ with coefficients little changed. Comparison with shear-only and shear-and-strain numerical simulations gives correlation coefficients $c_1 = 1.0 \times 10^{-8}$ and $r_2 = 25$ for the upper limit, $c_1 = 0.4 \times 10^{-8}$ and $r_2 = 10$ for the lower limit (Table 2). That lower-limit spectral transfer rates are smaller than the upper limit indicates that interactions with background scales smaller than those of the test wave do not average to zero in ray-tracing simulations.

Parameterization (6.1) compares favorably with previous shear- and strain-based scaling and Polzin *et al.*'s (1995) observations (Fig. 14). For the models, the ratio R_ω is varied by fixing the shear variance at its GM value and varying the strain variance. Observations are normalized by measured $\langle V_z^2 \rangle^{-2}$ to compensate for nonconstant shear spectral levels. Two points relevant to this as well as previous papers (Gregg 1989; Wijesekera *et al.* 1993; Polzin *et al.* 1995) must be stressed:

- extensions of GM-based parameterizations to non-GM spectral shapes have not been theoretically or numerically justified. All existing numerical or theoretical analyses are only applicable to exact GM spectra with $R_\omega = 3$.
- GM-based parameterizations [e.g., our (4.6) and (4.10); Henyey *et al.* 1986; McComas and Müller 1981b] can be arbitrarily rewritten in different forms (e.g., based on shear or strain variance) using relationships specific to GM model. While these alternate expressions agree with each other for GM spectral shapes, they give different predictions for ϵ if the internal wave field deviates from GM (for example, through varying shear-to-strain ratio, Fig. 14a).

With these two caveats in mind, Fig. 14 shows that Polzin *et al.*'s (1995) observations lie between the upper and lower limits of the shear-and-strain parameterization (6.1). Near the GM shear-to-strain ratio ($R_\omega = 2.9$), the observations agree with our upper limit and with McComas and Müller's (1981b) weak-triad predictions. They are significantly larger than Henyey *et al.* and Polzin *et al.*'s predictions. However, these data come from a decidedly non-GM wave field on the flanks of Fieberling Seamount where critical reflection and lee-wave generation elevate the high-frequency part of the spectrum (Eriksen 1998; Toole *et al.* 1997). Higher-than-GM shear-to-strain ratios are typical of the open ocean ($4.6 \leq R_\omega \leq 17$). That is, the ocean interior internal wave field is more inertial than the GM model. At these higher shear-to-strain ratios, the observations approach the lower limit of (6.1) and better agree with Polzin *et al.*'s extended model. Additional observations

are needed to test the parameterizations over a broader range of shear-to-strain ratio.

7. Discussion

Ray tracing has been used to study internal wave/wave interactions and estimate the rate of spectral energy transfer toward high vertical wavenumber and turbulence production (Henyey *et al.* 1986). Whether a test wave's evolution is controlled by background near-inertial shear or higher-frequency vertical divergence in this approach depends on its frequency compared to those of the dominant background shear and vertical divergence. Vertical divergence dominates the evolution of near-inertial waves even if only low-frequency vertical divergence is considered.

7.1 Comparison with Weak-Triad Method

7.1.1 Differences. The ray-tracing approach differs from weak-triad interaction theory in its assumptions and methodology for calculating the spectral energy transfer. Ray-tracing is not restricted to resonant-triad interactions. Nor does it require that the interaction timescale be long compared to the decorrelation timescale of internal wave field. However, ray-tracing does require that test waves be smaller than the background ($\Omega < \omega$, $K_i < k_i$) and that smallscale test waves not modify the larger-scale back-ground while weak-triad interaction theory does not have these limitations. Ambiguity in applying WKB scale-separation for $\Omega < \omega$, $K_i < k_i$ versus omitting some interactions introduces factor-of-two uncertainty in shear-only estimates of the spectral energy transfer rate, and factor-of-four uncertainty in shear-and-vertical-divergence estimates. It is also unclear whether the parametric subharmonic instability mechanism finds expression in the ray-tracing approach.

Ray tracing examines the energy transfer from large to small scales by following the evolution of smallscale test waves in GM background wave fields. Tracking the spectral action-flux of test waves leads to an estimate of the spectral energy transfer rate toward high vertical wavenumber. In the weak-triad method, spectral energy transfer through a fixed vertical wavenumber is calculated from the timescales for induced diffusion and parametric subharmonic instability.

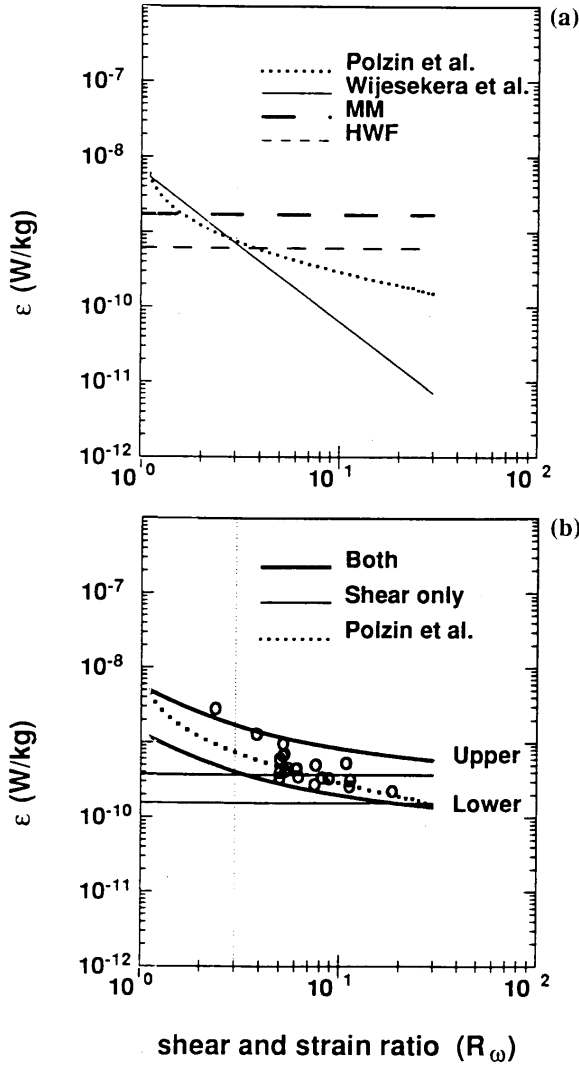


Figure 14. (a) Comparison of GM-based turbulent production models as functions of shear-to-strain ratio R_ω where shear variance is kept fixed at the GM value and strain varied. Models include strain-independent McComas and Müller (MM, 1981b) [thick dashed], strain-independent Henyey *et al.* (HWF, 1986) [thin dashed], shear- and strain-dependent Polzin *et al.* (PTS, 1995) [dotted], and strain-dependent Wijesekera *et al.* (WPDLP, 1993) [thin solid]. At non-GM shear-to-strain ratios, GM-based parameterizations are assumed valid without verification. (b) Comparison of upper and lower limits of shear-only parameterization (4.10) [thin horizontal lines], upper and lower limits of shear-and-strain parameterization (4.10) [thick solid curves], Polzin *et al.*'s (1995) observations (o) and Polzin *et al.*'s parameterization [dotted curve]. Observed dissipation rates have been normalized by $\langle V_z^2 \rangle^2 / \text{GM} \langle V_z^2 \rangle^2$ to compensate for nonconstant shear spectral levels. Observed ϵ fall between the upper and lower limits of our shear-and-strain parameterization, lying close to the lower limit and Polzin *et al.*'s parameterization for typical higher ratios.

7.1.2 Similarities. Despite differences in their assumptions and methodology, the results of ray-tracing and weak-triad interaction theory share

- low-frequency shear controlling the behavior of high-frequency waves and higher-frequency vertical divergence playing an important role in the evolution of near-inertial waves;
- net spectral energy transfer toward high vertical wavenumber; and
- similar dependence of the spectral transfer rate on buoyancy frequency and spectral energy levels.

Ray tracing provides a clear scenario of how background vertical divergence and shear affect smallscale test-wave behavior (Figs. 2–3). It reveals that low-frequency shear transports higher-frequency waves toward smaller scale and near-inertial frequency. Once near-inertial, vertical divergence acts most effectively to force finescale test waves toward breaking wavenumbers. Weak-triad interaction theory mathematically isolates the mechanisms of vertical divergence (PSI) and shear (ID) to represent total spectral energy transfer by the two triad interactions. However, as in the ray-tracing approach, these two transfer mechanisms are coupled. Induced diffusion first sends higher-frequency internal waves toward low frequency. Then parametric subharmonic instability transfers smallscale, low-frequency waves to even smaller scale. Thus, weak-triad interactions imply a similar physical scenario as ray tracing. We caution that, while there are broad similarities between ray-tracing and weak-triad results, there is no rigorous justification for equating the mechanisms in the two approaches.

7.2 Implications of Vertical Divergence Interactions

Inclusion of interactions with vertical divergence as well as shear leads to predicted turbulence production rates for a GM internal wave field that are 2–4 times larger than shear-only ray-tracing predictions (Henyey *et al.* 1986). This might resolve the discrepancy between observed dissipation rates and the shear-only parameterization in the presence of enhanced high-frequency wave activity (Padman *et al.* 1991; Wijesekera *et al.* 1993; Polzin *et al.* 1995). In these papers, strain was proposed to capture the high-frequency dynamics in turbulent production missed by shear-only models. The work presented here suggests that it is vertical divergence that is *physically* responsible for transferring energy to high wavenumber. However, if the reversible part of vertical wavenumber flux (dk_z/dt) due to high-frequency vertical divergence is filtered over during a test wave's lifespan, a parameterization for the turbulent production can be expressed in terms of shear

V_z and strain divided by the test-wave lifespan $\xi_z/\Delta t$ (4.10).

Recognizing the contribution from internal-wave vertical divergence in turbulence production may help understand the role of internal tides. At low and mid-latitudes, internal tides have intrinsic frequencies higher than f and much lower than N . They can have broad wavenumber ranges depending on the topography that generates them and the oceanic conditions they propagate through (Prinsenbergh and Rattray 1975; Baines 1982; New 1988). Based on discussions in this paper, we speculate that internal-tide vertical divergence might interact with smallscale near-inertial waves to produce intensified turbulence. This scenario is consistent with recent theoretical work on parametric subharmonic instability of internal tides by Hirst (1996) and observations by Sun *et al.* (1996).

8. Summary

Numerical simulation indicates that the internal-wave spectral energy transfer rate toward high vertical wavenumber is controlled by vertical divergence W_z as well as vertical shear V_z . For interactions with the total GM model spectrum (Munk 1981), ray-tracing calculations that include vertical divergence predict turbulence production rates four times those of a shear-only ray-tracing model (Heney *et al.* 1986) and observations. However, these estimates include interactions with background waves of higher horizontal wavenumber and frequency than the test waves, in violation of the WKB approximation. Confining interactions to background waves of larger vertical and horizontal scale, more commensurate with WKB scaling, reduces the shear-only contribution to ϵ by a factor of two and the shear-and-vertical-divergence contribution by a factor of four, implying shear-and-strain production rates consistent with upper-limit shear-only values (Heney *et al.* 1986) and observations (Gregg 1989; Polzin *et al.* 1995).

A number of assumptions have been made for our ray-tracing internal wave/wave interactions. Fundamental to the ray-tracing approach are

- dominance of scale-separated wave/wave interactions so that the WKB approximation ($\lambda < \Lambda$) is applicable;
- smallscale test waves not significantly modifying the background.

The degree of scale-separation necessary for the validity of the WKB results is uncertain. As a sizable fraction of the net spectral energy transfer is associated with finescale waves that are not well scale-separated ($k_z \simeq K_z$), this leads to uncertainty in quantitative estimates from the ray-tracing approach.

Following Heney *et al.* (1986), Gregg (1989) and Polzin *et al.* (1995), we have assumed that

- the net rate of spectral energy transfer toward high vertical wavenumber is identical to the turbulence production rate $\epsilon(1 + \gamma)$;
- the turbulence production rate can be parameterized in terms of shear and strain variances;
- background vertical shear V_z and vertical divergence W_z are uncorrelated;
- all test waves lose their energy to turbulence when their vertical wavelength λ_z is forced below 5 m —simulations show little sensitivity to the breaking wavenumber;
- the spectral action-flux can be expressed with (5.1);
- finescale test-wave behavior can be described by the linear internal-wave dispersion relation.

The Munk (1981) version of the GM model spectrum was assumed to adequately describe the finescale internal wave field. This implies:

- the internal-wave spectrum is separable in frequency and vertical wavenumber so that shear, strain and vertical divergence variances are dominated by the same high vertical wavenumber band;
- for wavenumbers, $k_z < k_{z_c} = 0.08$ cpm, the internal-wave energy density spectrum has k_z^{-2} dependence on vertical wavenumber and ω^{-2} dependence on frequency so that shear is dominated by near-inertial frequencies, strain by higher but still low frequencies, and vertical divergence by high frequencies;
- at fine scales, $k_z > k_{z_c} = 0.08$ cpm, the energy density spectra has a k_z^{-3} dependence on vertical wavenumber, but the same ω^{-2} intrinsic frequency dependence as at lower wavenumber.

The Munk model has less finescale variance than the GM76 model (Gregg and Kunze 1991). The intrinsic frequency spectrum is not well-known at the finescale because of Doppler-shifting (Kunze *et al.* 1990; Sherman and Pinkel 1991; Anderson 1993). Figures 4 and 5 suggest that the equilibrium finescale frequency spectrum may have a gentler slope than GM.

Unlike previous ray-tracing internal wave/wave investigations, we have

- included interactions with background internal wave vertical divergence,
- used test-wave lifespan averages to filter out the highest frequency contributions to the vertical divergence, and

- explored the consequences of applying WKB scale-separation to the horizontal wavenumbers $K_H < k_h$ for background frequencies $\Omega > 11f$.

Parameterizations (4.6) and (6.1) [derived from (4.10)] of the turbulence production rate $\epsilon(1 + \gamma)$ were proposed for GM spectral shapes with coefficients deduced from numerical ray-tracing simulations. Equation (4.6) expresses the turbulence production rate in terms of shear and vertical divergence. It assumes that total GM variances contribute to spectral energy transfer.

Since some high-frequency vertical divergence effects may be reversible over test-wave lifespans, and the simulations do not satisfy WKB scale-separation in the horizontal or time, (4.6) is likely an overestimate. To account for averages over test-wave lifespans, (6.1) expresses the turbulence production rate in terms of shear and strain. Two sets of coefficients were obtained for (6.1) from numerical simulations: an upper limit where interactions are allowed with the total background GM wave field except background vertical wavenumbers $K_z > k_z$, and a lower limit restricting background vertical wavenumbers $K_z < 0.5k_z$ and horizontal wavenumbers $K_H < k_h$ for frequencies $\Omega > 11f$. Application of strict WKB scale-separation, $K_H < k_h$ or $\Omega < \omega$, caused a significant fraction of test waves to stall at low k_h and low ω before reaching the breaking wavenumber. Thus, strict WKB scale-separation cannot be realistically applied to the wave/wave ray-tracing problem. The above lower-limit criteria are used as a compromise.

We speculate that the lower-limit predictions from (6.1) are more realistic because they exclude reversible high-frequency contributions, are more consistent with WKB scale-separation, and are consistent with ocean interior observations (Fig. 14b). This is by no means certain, however, because interactions between finescale test waves and finescale backgrounds that cannot be described reliably under the WKB approximation may contribute a significant fraction of the total spectral energy transfer. This introduces a factor-of-four uncertainty in the shear-and-strain turbulence production rate estimates, and factor-of-two uncertainty in the shear-only estimates. While our upper-limit turbulence production rates are consistent with weak-triad results (McComas and Müller 1981b), weak-triad assumptions likewise break down on the finescale.

Although shear and vertical divergence are physically responsible for transferring internal waves to smaller scales (through dk_z/dt), it is unclear whether shear, strain (or vertical divergence) variances are sufficient to parameterize the spectral energy transfer rate $\epsilon(1 + \gamma)$. Both our numerical simulations and weak-triad interactions (McComas and Bretherton 1977) suggest that it is

not be the highest frequency vertical divergence (section 4), nor the smallest-scale shear and vertical divergence (Fig. 13), that are most effective in transferring energy toward high vertical wavenumbers. The frequency- (section 4) and wavenumber-contents (Fig. 13) of the variances are also important. Our results, and those of Polzin *et al.* (1995), suggest that turbulence production is more sensitive to frequency-content. Nevertheless, it may be necessary to know frequency spectral shapes for shear and vertical divergence, and the degree of separability of the vertical wavenumber/frequency spectra, to accurately parameterize the turbulent production rate for the broad range of internal wave fields found in the ocean. Unfortunately, the fine-scale intrinsic frequency spectrum is difficult to measure directly because of both vertical and horizontal Doppler-smearing (Kunze *et al.* 1990; Sherman and Pinkel 1991; Anderson 1993; Sun *et al.* 1996).

This paper suggest a significant role for low-frequency vertical divergence in the production of turbulence. Parameterization (6.1) in principle incorporates non-GM spectral shapes and compares favorably with observations (Fig. 14b). However, further work is needed to address the above issues and develop a robust turbulent production rate parameterization for the range of non-GM internal wave spectral shapes found in the ocean. Without a robust approach for treating oceanic internal wave/wave interactions, the lower-limit parameterization is our best estimate. But it should be applied to non-GM fields with caution. Numerical primitive-equation models are one promising approach. Although not yet able to span the full range of scales involved in oceanic internal waves, Winters and D’Asaro (1997) found spectral energy transfer rates consistent with observations and our lower-limit estimates.

Acknowledgments. We are grateful to Frank Henyey for providing the basic numerical simulation code and much helpful guidance. We acknowledge valuable discussions with Kurt Polzin, Eric D’Asaro, Jim Riley, and Kraig Winter. This work is based on Haili Sun’s Ph.D. dissertation and two accepted papers (Sun and Kunze 1999a,b) which were supported by NSF grant OCE 94-16056.

Appendix A: Scaling the Nonlinear Terms in the Equations of Motion

In this appendix, we scale the internal-wave equations of motion to determine which nonlinearities dominate the evolution of finescale waves in a GM background field. The scaling will assume the finescale motions scale with the internal-wave dispersion relation. This is not strictly

correct but is a reasonable starting point (Fig. A1). The following relations will be used

$$\frac{w}{u} \sim \frac{k_h}{k_z} = \frac{\sqrt{\omega^2 - f^2}}{\sqrt{N^2 - \omega^2}} \quad (\text{A1})$$

from continuity and the linear dispersion relation,

$$\frac{b}{u} \sim \frac{N^2 w}{\omega u} \sim \frac{N^2}{\omega} \sqrt{\frac{\omega^2 - f^2}{N^2 - \omega^2}} \quad (\text{A2})$$

from conservation of buoyancy and the linear dispersion relation, and

$$\frac{p}{u} \sim \frac{\sqrt{N^2 - \omega^2} \sqrt{\omega^2 - f^2}}{\omega k_z} \quad (\text{A3})$$

from conservation of vertical momentum.

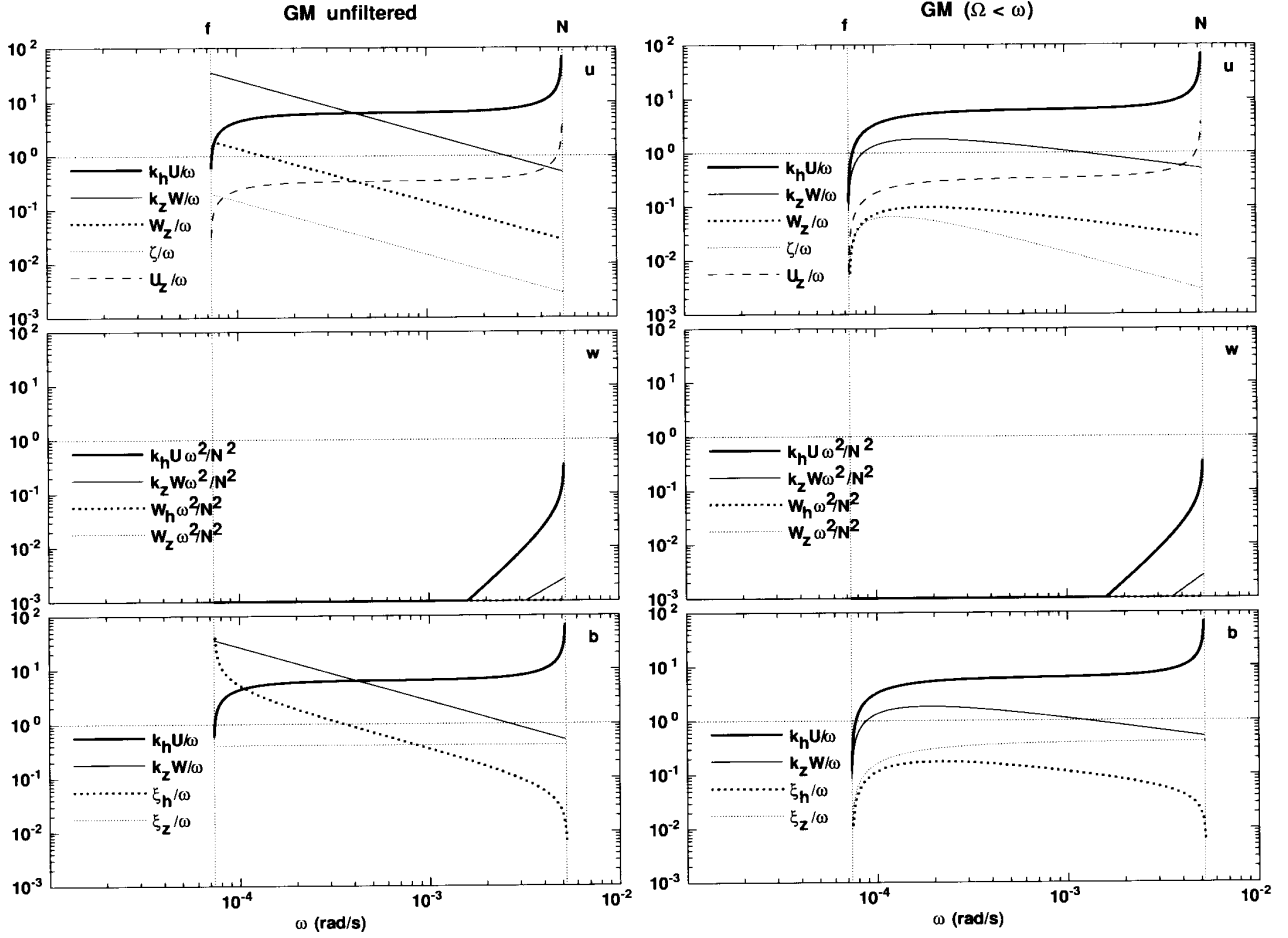


Figure A1. The normalized magnitude of nonlinear terms as a function of test-wave intrinsic frequency ω for a 10-m vertical wavelength test wave in a GM background internal wave field. Magnitudes are shown for nonlinear terms in conservation of horizontal momentum [upper panels, (A4)], vertical momentum [center panels, (A5)] and buoyancy [lower panels, (A6)]. In left panels, unfiltered rms backgrounds are used (all frequencies and horizontal wavenumbers), constrained only by the background vertical wavenumber being lower than the test wave's, $K_z < k_z$. In right panels, temporal filtering is applied ($\Omega < \omega$); this also guarantees horizontal filtering. In all cases, advection (solid curves) dominates over background gradient terms (dotted and dashed). In the strict WKB-filtered case (right panels), horizontal advection is 3–8 times larger than vertical advection and test-wave intrinsic frequency except at very near-inertial frequencies.

A.1 Horizontal Momentum

The zonal momentum balance can be expressed

$$u_t + (\mathbf{V}_H \cdot \nabla)u + Wu_z + U_x u + U_y v \\ + U_z w - fv = -p_x$$

where lowercase variables represent the finescale test wave and uppercase the background wave field. The meridional conservation equation is similar. Substituting wave-like solutions and normalizing by the time rate of change, individual terms scale as

$$1; \frac{Uk_z}{\omega} \sqrt{\frac{\omega^2 - f^2}{N^2 - \omega^2}}; \frac{Wk_z}{\omega}; \frac{W_z}{2\omega}; \frac{\zeta}{2\omega}; \\ \frac{V_z}{2\omega} \sqrt{\frac{\omega^2 - f^2}{N^2 - \omega^2}}; \frac{f}{\omega} \sim \frac{N^2}{\omega^2} \frac{\omega^2 - f^2}{N^2 - \omega^2} \quad (\text{A4})$$

where U represents the background horizontal velocity, W the background vertical velocity, $-W_z$ the background horizontal divergence, ζ the rms vertical vorticity and V_z the background vertical shear. The second through sixth terms are nonlinear.

A.2 Vertical Momentum

The vertical momentum balance can be expressed

$$w_t + (\mathbf{V}_H \cdot \nabla)w + Ww_z + W_x u + W_y v + W_z w \\ = -p_z + b.$$

which scales as

$$\frac{\omega^2}{N^2}; \frac{\omega Uk_z}{N^2} \sqrt{\frac{\omega^2 - f^2}{N^2 - \omega^2}}; \frac{\omega Wk_z}{N^2}; \\ \frac{\omega \nabla_H W}{N^2} \sqrt{\frac{N^2 - \omega^2}{\omega^2 - f^2}}; \frac{\omega W_z}{N^2} \sim \sqrt{\frac{\omega^2 - f^2}{N^2 - \omega^2}}; 1 \quad (\text{A5})$$

where $\nabla_H W$ represents the background horizontal shear of vertical velocity and W_z the background vertical divergence.

A.3 Buoyancy

Conservation of buoyancy can be expressed

$$b_t + (\mathbf{V}_H \cdot \nabla)b + Wb_z + B_x u + B_y v \\ + N^2 w - N^2 Z_z w = 0$$

which scales as

$$1; \frac{Uk_z}{\omega} \sqrt{\frac{\omega^2 - f^2}{N^2 - \omega^2}}; \frac{Wk_z}{\omega}; \nabla_H Z \sqrt{\frac{N^2 - \omega^2}{\omega^2 - f^2}}; \\ 1; Z_z \sim 0 \quad (\text{A6})$$

where $\nabla_H Z$ represents the background isopycnal slope and Z_z the background vertical strain.

Figure A1 displays the magnitudes of the nonlinear terms in (A4–A6) as functions of test-wave intrinsic frequency ω . Background quantities were estimated as rms values from the Munk (1981) GM model spectrum. Test-wave wavenumber is $k_z = 2\pi/10$ m. Two cases are displayed. The ‘unfiltered’ case satisfies the vertical WKB constraint only (left panels) with background vertical wavenumber $K_z < k_z$. The ‘filtered’ additionally satisfies the temporal WKB constraint $\Omega < \omega$ (right panels, filtered).

Temporal and horizontal WKB approximation are both satisfied by choosing $\Omega < \omega$. From the internal-wave dispersion relation

$$K_H = \sqrt{\frac{\Omega^2 - f^2}{N^2 - \Omega^2}} K_z < \sqrt{\frac{\omega^2 - f^2}{N^2 - \omega^2}} k_z = k_h \quad (\text{A7})$$

provided $K_z < k_z$ and $\Omega < \omega$; $\Omega < \omega$ implies numerators $(\Omega^2 - f^2) < (\omega^2 - f^2)$ and denominators $(N^2 - \Omega^2) > (N^2 - \omega^2)$.

The vertical momentum equation is linear for all frequencies (Fig. A1). In both the filtered and unfiltered cases, advective nonlinear terms in the horizontal momentum and buoyancy equations exceed the intrinsic frequency by factors of at least 5 (except for very-near-inertial waves in the filtered case). This demonstrates that advection by background internal waves greatly exceeds the phase and group velocities of finescale internal waves at all but very-near-inertial frequencies. In the WKB-filtered case, horizontal advection dominates over vertical advection by factors of 3–30. While smaller than horizontal advection, vertical advection is significant at lower test-wave frequencies. Deforming or gradient nonlinear terms are smaller. In the unfiltered case, vertical divergence, vertical shearing and isopycnal tilting exceed the intrinsic frequency in different frequency bands. In a Lagrangian frame, where advection is absent, only vertical shearing and straining compare to the intrinsic frequency in magnitude for the WKB frequency scale-separated case.

Appendix B: Monte-Carlo Simulations of a Garrett-Munk Internal Wave Field

Density spectra can be treated as a probability density functions using Monte-Carlo methods (Bouveau and Lepingle 1993) to find random sampling schemes for

background wave frequency Ω , mode number j , and amplitude \mathbf{V}_0 in such a way as to reproduce the GM model spectrum for horizontal velocity (3.1).

B.1 Sampling Frequency Ω

The frequency dependence of (3.1) contains two terms, $(1 + f^2/\Omega^2)$ and $1/\Omega/\sqrt{\Omega^2 - f^2}$. We will utilize the first term to constrain the amplitudes of the U and V components based on the equations of motion for linear internal waves on the rotating earth. The second term will be used for the Monte-Carlo selection of wave frequencies. Integrating and normalizing the second term,

$$\frac{\int_f^{\Omega} \frac{d\Omega}{\Omega \sqrt{\Omega^2 - f^2}}}{\int_f^{N_0} \frac{d\Omega}{\Omega \sqrt{\Omega^2 - f^2}}} = \frac{\cos\left(\frac{f}{\Omega}\right)}{\cos\left(\frac{f}{N_0}\right)} = \text{rnd}(e_1) \quad (\text{B1})$$

where $\text{rnd}(e_1)$ represents a random number in $[0, 1]$. In the following, we will use $\text{rnd}(e_1)$, $\text{rnd}(e_2)$...to indicate different random number sequences. Inverting (B1) for Ω , the sample scheme for background wave frequencies should be

$$\Omega = \frac{f}{\text{Arcos}[\cos(f/N_0)\text{rnd}(e_1)]} \quad (\text{B2})$$

B.2 Sampling Mode Number j

For numerical efficiency, mode numbers for background waves are divided into low ($j_* < j < j_{\text{sep}}$, $j_{\text{sep}} = 10$) and high ($j_{\text{sep}} < j < j_c$) mode number regimes. Low mode numbers, which dominate the background kinetic energy, are more densely sampled than high mode numbers. As with the frequency sampling (B2), we invert the normalized integration of the vertical mode number spectral shape

$$\frac{\int_{j_*}^j \frac{dj}{j^2 + j_*^2}}{\int_{j_*}^{j_{\text{sep}}} \frac{dj}{j^2 + j_*^2}} = \frac{\text{Arctan} \frac{j}{j_*} \frac{\pi}{4}}{\text{Arc tan} \frac{j_{\text{sep}}}{j_*} \frac{\pi}{4}} \text{rnd}(e_2) \quad (\text{B3})$$

for j . The sampling scheme for low mode number j is then

$$j = j_* \tan \left[\frac{\pi}{4} + \text{Arctan}(j_{\text{sep}}/j_*) \text{rnd}(e_2) \right] \approx j_* \tan \left[\text{Arctan}(j_{\text{sep}}/j_*) \text{rnd}(e_2) \right] \quad (\text{B4})$$

for $j_* < j < j_{\text{sep}}$. Similarly, the sampling scheme for high mode number j is

$$j = j_{\text{sep}} \tan \left[\frac{\pi}{4} + \text{Arctan}(j_c/j_{\text{sep}}) \text{rnd}(e_3) \right] \approx j_{\text{sep}} \tan \left[\text{Arctan}(j_c/j_{\text{sep}}) \text{rnd}(e_3) \right] \quad (\text{B5})$$

for $j_{\text{sep}} < j < j_c$.

After selecting wave frequency Ω and mode number j , the horizontal wavenumber is determined from the internal-wave dispersion relation, with the direction of horizontal wavevector $\theta = \text{Arctan}(K_y/K_x)$ randomly chosen from $[0, 2\pi]$ to ensure horizontal isotropy.

B.3 Sampling Wave Amplitude

Background wave horizontal velocity amplitudes are sampled according to an exponential law approximating a Gaussian distribution (Briscoe 1977), i.e.,

$$\mathbf{V}_0 = C \sqrt{\frac{2 \text{Arctan}(j_{\text{sep}}/j_*)}{\pi n_1}} \sqrt{-2 \ln[\text{rnd}(e_4)]} \quad \text{for } j < j_{\text{sep}} \\ = C \sqrt{\frac{2 \text{Arctan}(j_c/j_{\text{sep}})}{\pi n_2}} \sqrt{-2 \ln[\text{rnd}(e_5)]} \quad \text{for } j > j_{\text{sep}} \quad (\text{B6})$$

where coefficient $C = b \sqrt{N_0 NE_{\text{GM}}}$, n_1 and n_2 are the numbers of low and high mode-number waves selected in the Monte-Carlo process, respectively, such that $n_1 + n_2 = NW$, NW being the total number of background waves selected for the Monte-Carlo simulation.

Having selected NW wave frequencies Ω , vertical wavenumbers K_z and amplitudes \mathbf{V}_0 , we can construct the 3-D wave field with Lagrangian variables (x' , y' , z' (ρ), t'). Defining the horizontal phase, vertical phase and horizontal propagation direction

$$\phi = K_x x' + K_y y' - \Omega t'$$

$$\psi = K_z z' = \frac{j\pi}{b} \sqrt{\frac{N^2 - \Omega^2}{N_0^2 - \Omega^2}} z'$$

$$\theta = \text{Arctan} \left(\frac{K_y}{K_x} \right) = 2\pi \text{rnd}(e_6)$$

then

$$U = \sum_{n=1}^{NW} (U_{rx} \cos \phi - U_{ix} \sin \phi) \cos \psi \quad (\text{B7})$$

$$V = \sum_{n=1}^{NW} (V_{ry} \cos \phi - V_{iy} \sin \phi) \cos \psi \quad (\text{B8})$$

where the amplitudes are

$$U_{rx} = \mathbf{V}_0 \left[\frac{K_x}{K_h} \cos\theta + \frac{f}{\Omega} \frac{K_y}{K_h} \sin\theta \right] \quad (\text{B9})$$

$$U_{ix} = \mathbf{V}_0 \left[\frac{K_x}{K_h} \sin\theta - \frac{f}{\Omega} \frac{K_y}{K_h} \cos\theta \right] \quad (\text{B10})$$

$$V_{ry} = \mathbf{V}_0 \left[\frac{K_y}{K_h} \cos\theta - \frac{f}{\Omega} \frac{K_x}{K_h} \sin\theta \right] \quad (\text{B11})$$

$$V_{iy} = \mathbf{V}_0 \left[\frac{K_y}{K_h} \sin\theta + \frac{f}{\Omega} \frac{K_x}{K_h} \cos\theta \right] \quad (\text{B12})$$

The simulated background spectra reproduce the GM model spectrum (Fig. 1).

Appendix C: Coordinate Transformations

Here, we transform the ray-tracing equations into a semi-Lagrangian frame following wave-induced vertical displacements of isopycnals ξ but not horizontal internal-wave displacements χ and η . Assuming x', y', z', t' are Lagrangian variables, and x, y, z, t Eulerian, the semi-Lagrangian transform is

$$x' = x, y' = y, z' = z - \xi, t' = t$$

where the vertical displacement $\xi = \xi_0(x', y', z', t')$. The transformed derivatives are

$$\frac{\partial}{\partial x} = \frac{\partial}{\partial x'} - s \frac{\partial}{\partial z'} \xi_{x'}$$

$$\frac{\partial}{\partial y} = \frac{\partial}{\partial y'} - s \frac{\partial}{\partial z'} \xi_{y'}$$

$$\frac{\partial}{\partial z} = s \frac{\partial}{\partial z'}$$

$$\frac{\partial}{\partial t} = \frac{\partial}{\partial t'} - s \frac{\partial}{\partial z'} \xi_{t'}$$

where the Jacobian of the transformation is $s = 1/(1 + \xi_{z'})$. After transforming, the ray equations become

$$\frac{d'x'}{d't} = \frac{\partial \omega_i}{\partial k_x} + U \quad (\text{C1})$$

$$\frac{d'y'}{d't} = \frac{\partial \omega_i}{\partial k_y} + V \quad (\text{C2})$$

$$\frac{d'z'}{d't} = \frac{\partial \omega_i}{\partial k_z} \quad (\text{C3})$$

$$\frac{d'k_x}{d't} = - \frac{\partial \omega_i}{\partial N_i} \frac{\partial N_i}{\partial x'} - k_x U_{x'} - k_y V_{x'} - k_z W_{x'} \quad (\text{C4})$$

$$+ s \xi_{x'} \left[\frac{\partial \omega_i}{\partial N_i} \frac{\partial N_i}{\partial z'} + k_x U_{z'} + k_y V_{z'} + k_z W_{z'} \right]$$

$$\frac{d'k_y}{d't} = - \frac{\partial \omega_i}{\partial N_i} \frac{\partial N_i}{\partial y'} - k_x U_{y'} - k_y V_{y'} - k_z W_{y'} \quad (\text{C5})$$

$$+ s \xi_{y'} \left[\frac{\partial \omega_i}{\partial N_i} \frac{\partial N_i}{\partial z'} + k_x U_{z'} + k_y V_{z'} + k_z W_{z'} \right]$$

$$\frac{d'k_z}{d't} = - s \left[\frac{\partial \omega_i}{\partial N_i} \frac{\partial N_i}{\partial z'} + k_x U_{z'} + k_y V_{z'} + k_z W_{z'} \right] \quad (\text{C6})$$

Here, $N_i^z = N^2(1 + \xi_{z'})$ is the instantaneous buoyancy frequency squared, $N = N_0 e^{z/b}$ the background buoyancy frequency, $d'/d't$ the ray-following time derivative in semi-Lagrangian coordinates, and

$$\frac{\partial N_i}{\partial x'} = \frac{N^2}{2N_i} \xi_{x'z'}$$

$$\frac{\partial N_i}{\partial y'} = \frac{N^2}{2N_i} \xi_{y'z'}$$

$$\frac{\partial N_i}{\partial z'} = \frac{N^2}{2N_i} \xi_{z'z'} + \frac{N}{N_i} \frac{\partial N}{\partial z'} (1 + \xi_{z'})$$

where x', y', z' are Lagrangian variables following the vertical movement of the water.

Appendix D: GM Shear, Strain, Vertical Divergence and Action Spectra

The background GM shear, strain and vertical divergence spectra following Munk (1981) are

$$S[\mathbf{V}_z](\Omega, K_z) = \frac{\pi}{b} A(\Omega) \frac{K_z^2 dK_z}{K_z^2 + K_z^*}$$

$$S[\xi_z](\Omega, K_z) = \frac{1}{N^2} \frac{\Omega^2 - f^2}{\Omega^2 + f^2} \cdot S[\mathbf{V}_z](\Omega, K_z)$$

$$S[W_z](\Omega, K_z) = \frac{\Omega^2}{N^2} \frac{\Omega^2 - f^2}{\Omega^2 + f^2} \cdot S[\mathbf{V}_z](\Omega, K_z)$$

where the frequency spectrum

$$A(\Omega) = \frac{4b^2 j^* f N_0 N^2 E_{\text{GM}}}{\pi^2} \left(1 + \frac{f^2}{\Omega^2} \right) \frac{1}{\Omega \sqrt{\Omega^2 - f^2}}$$

To compare test-wave action density spectra with the GM model, and to assign test waves an initial spectral action flux in section 3, the GM action density spectra

$$\begin{aligned}
 S[A](k_h, k_z, z) &= S[E/\omega](k_h, k_z, z) \\
 &= \frac{4j_* b f N^2 E_{\text{GM}}}{\pi} \frac{k_z^2}{k_z^2 + k_{z*}^2} \frac{\sqrt{N(z)^2 - f^2}}{[N(z)^2 k_h^2 + f^2 k_z^2]^{3/2}}
 \end{aligned}$$

References

- Alford, M., and R. Pinkel, 1999: Observations of overturning in the thermocline: The context of ocean mixing. *J. Phys. Oceanogr.*, submitted.
- Anderson, S.P., 1993: Shear, strain and thermohaline vertical shear in the upper ocean. Ph.D. thesis, University of California, San Diego, 143 pp.
- Baines, P.G., 1982: On internal tide generation models. *Deep-Sea Res.*, **29**, 307–338.
- Bouleau, N., and D. Lepingle, 1993: Numerical methods for stochastic processes. John Wiley and Sons, New York, 351 pp.
- Briscoe, M.G., 1977: Gaussianity of internal waves. *J. Geophys. Res.*, **82**, 2117–2126.
- Cairns, J.L., and G.O. Williams, 1976: Internal wave observations from a midwater float, 2. *J. Geophys. Res.*, **81**, 1943–1950.
- Duda, T.F. and C.S. Cox, 1989: Vertical wave number spectra of velocity and shear at small internal wave scales, *J. Geophys. Res.*, **94**, 939–950.
- Eriksen, C.C., 1978: Measurements and models of finestructure, internal gravity waves, and wave breaking in the deep ocean. *J. Geophys. Res.*, **83**, 2989–3009.
- Eriksen, C.C., 1998: Internal wave reflection and mixing at Fieberling Guyot. *J. Geophys. Res.*, **103**, 2977–2994.
- Fofonoff, N.P., 1969: Spectral characteristics of internal waves in the ocean. *Deep-Sea Res.*, **16**(Suppl.), 58–71.
- Gargett, A.E., 1990: Do we really know how to scale the turbulent kinetic energy dissipation rate ϵ due to breaking of oceanic internal waves? *J. Geophys. Res.*, **95**, 15,971–15,974.
- Gargett, A.E., P.J. Hendricks, T.B. Sanford, T.R. Osborn, and A.J. Williams III, 1981: A composite spectrum of vertical shear in the ocean. *J. Phys. Oceanogr.*, **11**, 1258–1271.
- Gregg, M.C., and E. Kunze, 1991: Internal wave shear and strain in Santa Monica basin. *J. Geophys. Res.*, **96**, 16,709–16,719.
- Gregg, M.C., D.P. Winkel, and T.B. Sanford, 1993: Varieties of fully resolved spectra of vertical shear. *J. Phys. Oceanogr.*, **23**, 124–141.
- Gregg, M.C., E.A. D'Asaro, T.J. Shay, and N. Larson, 1986: Observations of persistent mixing and near-inertial internal waves. *J. Phys. Oceanogr.*, **16**, 856–885.
- Gregg, M.C., 1987: Diapynal mixing in the thermocline: A review. *J. Geophys. Res.*, **92**, 5249–5286.
- Gregg, M.C., 1989: Scaling turbulent dissipation in the thermocline. *J. Geophys. Res.*, **94**, 9686–9698.
- Haynes, P., and J. Anglade, 1997: Vertical-scale cascade in atmospheric tracers due to large-scale differential advection. *J. Atmos. Sci.*, **54**, 1121–1136.
- Henye, F.S., 1984: Transport of small-scale internal waves toward microstructure. *Proc. 'Aha Huliko'a Hawaiian Winter Workshop*, P. Müller and D. Henderson, Eds., U. of Hawaii, Honolulu, pp. 201–219.
- Henye, F.S., J. Wright, and S.M. Flatté, 1986: Energy and action flow through the internal wave field: An eikonal approach. *J. Geophys. Res.*, **91**, 8487–8495.
- Henye, F.S., 1991: Scaling of internal wave model predictions for ϵ . *Proc. 'Aha Huliko'a Hawaiian Winter Workshop*, P. Müller and D. Henderson, Eds., U. Hawaii, Honolulu, pp. 233–236.
- Hines, C.O., 1991: The saturation of gravity waves in the middle atmosphere. Part II: Development of Doppler-spread theory. *J. Atmos. Sci.*, **48**, 1360–1379.
- Hirst, E.V., 1996: Resonant instability of internal tides. Ph.D. thesis, University of Washington, Seattle, WA, 92 pp.
- Holloway, G., 1980: Oceanic internal waves are not weak waves. *J. Phys. Oceanogr.*, **10**, 906–914.
- Itsweire, E.C., K.N. Helland and C.W. Van Atta, 1986: The evolution of grid-generated turbulence in a stably stratified fluid. *J. Fluid Mech.*, **162**, 299–238.
- Kunze, E., A.J. Williams III and M.G. Briscoe, 1990: Observations of shear and vertical stability from a neutrally buoyant float. *J. Geophys. Res.*, **95**, 18,127–18,142.
- Leaman, K.D., and T.B. Sanford, 1975: Vertical energy propagation of inertial waves: A vector spectral analysis of velocity profiles. *J. Geophys. Res.*, **80**, 1975–1978.
- Lighthill, J., 1978: *Waves in Fluids*. Cambridge University Press, Cambridge, 504 pp.
- McComas, C. H., and F.P. Bretherton, 1977: Resonant interactions of oceanic internal waves. *J. Geophys. Res.*, **83**, 1397–1412.
- McComas, C.H., and P. Müller, 1981a: Time scales of resonant interactions among oceanic internal waves. *J. Phys. Oceanogr.*, **11**, 139–147.
- McComas, C.H., and P. Müller, 1981b: The dynamic balance of internal waves. *J. Phys. Oceanogr.*, **11**, 970–986.
- McEwan, A.D., 1983: Internal mixing in stratified fluids. *J. Fluid Mech.*, **128**, 59–80.
- Müller, P., G. Holloway, F. Henye and N. Pomphrey, 1986: Non-linear interactions among internal gravity waves. *Rev. Geophys.*, **24**, 493–536.
- Munk, W., 1981: Internal waves and small-scale processes. *Evolution of Physical Oceanography*, B.A. Warren and C. Wunsch, Eds., The MIT Press, pp. 264–291.
- New, A.L., 1988: Internal tidal mixing in the Bay of Biscay. *Deep-Sea Res.*, **35**, 691–709.
- Oakey, N.S., 1982: Determination of the rate of dissipation of turbulent kinetic energy from simultaneous temperature and velocity shear microstructure measurements. *J. Phys. Oceanogr.*, **12**, 256–271.
- Osborn, T.R., 1980: Estimates of the local rate of vertical diffusion from dissipation measurements. *J. Phys. Oceanogr.*, **10**, 83–89.
- Padman, L., T.M. Dillon, H.W. Wijesekera, M.D. Levine, C.A. Paulson and R. Pinkel, 1991: Internal wave dissipation in a non-Garrett-Munk ocean. *Proc. 'Aha Huliko'a Hawaiian Winter Workshop*, P. Müller and D. Henderson, Eds., U. of Hawaii, Honolulu, pp. 31–51.
- Pinkel, R., 1984: Doppler sonar observations of internal waves: The wavenumber-frequency spectrum. *J. Phys. Oceanogr.*, **14**, 1249–1270.
- Polzin, K., J.M. Toole and R.W. Schmitt, 1995: Finescale parameterizations of turbulent dissipation. *J. Phys. Oceanogr.*, **25**, 306–328.

- Prinsenbergh, S.J. and M. Rattray, 1975: Effects of continental slope and variable Brunt-Vaisala frequency on the coastal generation of internal tides. *Deep-Sea Res.*, **22**, 251–263.
- Sherman, J.T., and R. Pinkel, 1991: Estimates of the vertical wavenumber-frequency spectra of vertical shear and strain. *J. Phys. Oceanogr.*, **21**, 292–303.
- Smith, S.A., D.C. Fritts and T.E. Van Zandt, 1987: Evidence of a saturation spectrum of atmospheric gravity waves. *J. Atmos. Sci.*, **44**, 1404–1410.
- Sun, H., E. Kunze and A.J. Williams III, 1996: Vertical heat-flux measurements from a neutrally buoyant float. *J. Phys. Oceanogr.*, **26**, 984–1001.
- Sun, H., and E. Kunze, 1999a: Internal wave/wave interactions: Part I. The role of internal wave vertical divergence. *J. Phys. Oceanogr.*, **29**, in press.
- Sun, H. and E. Kunze, 1999b: Internal wave/wave interactions: Part II. Spectral energy transfer and turbulence production. *J. Phys. Oceanogr.*, **29**, in press.
- Thompson, R.O.R.Y., 1980: Efficiency of conversion of kinetic to potential energy by a breaking internal gravity waves. *J. Geophys. Res.*, **85**, 6631–6635.
- Toole, J.M., R.W. Schmitt, K.L. Polzin and E. Kunze, 1997: Near-boundary mixing above the flanks of a mid-latitude seamount. *J. Geophys. Res.*, **102**, 947–959.
- Wijesekera, H., L. Padman, T. Dillon, M. Levine, C. Paulson and R. Pinkel, 1993: The application of internal-wave dissipation models to a region of strong mixing. *J. Phys. Oceanogr.*, **23**, 269–286.
- Winters, K.B., and E.A. D’Asaro, 1997: Direct simulation of internal wave energy transfer. *J. Phys. Oceanogr.*, **27**, 1937–1945.